Elemental-Doped Catalysts for Photoelectrochemical CO_2 Conversion to Solar Fuels

Elemental-doped catalysts for photoelectrochemical CO_2 conversion to solar fuels

Chaitanya B. Hiragond, Jungmyung Kim, Hwapyong Kim, Dowon Bae, Su-Il In**

C. B. Hiragond, H. Kim, and S.-I. In
Department of Energy Science & Engineering, Daegu Gyeongbuk Institute of Science and Technology (DGIST), 333 Techno Jungang-daero, Hyeonpung-eup, Dalseong-gun, Daegu, 42988, Republic of Korea.

J. Kim and D. Bae
Institute of Mechanical, Process and Energy Engineering (IMPEE), School of Engineering and Physical Sciences, Heriot-Watt University, Edinburgh, EH14 4AS, UK.

D. Bae
Wolfson School of Mechanical, Electrical and Manufacturing Engineering, Loughborough University, Loughborough, Leicestershire, LE11 3TU, UK.

S.-I. In
Materials and Process Simulation Center, California Institute of Technology, Pasadena, CA, 91125, United States.

Email: Dowon Bae (d.bae@lboro.ac.uk) and Su-Il In (insuil@dgist.ac.kr)

Keywords: Photoelectrochemical cell (PEC), CO_2 reduction, metal-doped photoelectrodes, non-metal-doped photoelectrodes, Solar to fuel

Solar-driven photoelectrochemical (PEC) CO_2 conversion to valuable chemicals, combining the advantages of photocatalysis and electrocatalysis, represents a promising approach towards establishing a carbon-neutral society and harnessing solar energy. Photoelectrode materials doped with metals and/or non-metals have shown promise in achieving high CO_2 reduction efficiency. Metal or non-metal doping entails introducing a heteroelement into the semiconductor, thereby

modifying the band potentials of the semiconductor through the addition of a defective state. This alteration may improve the charge transfer kinetics of the catalysis. Furthermore, doping aids in creating active CO_2 adsorption offers anchoring sites for CO_2 molecules, and can promote product selectivity. This review aims to provide a concise summary of elemental-doped photoelectrodes for converting CO_2 into fuels through photoelectrochemical processes. We discuss several key factors affecting the performance of PEC CO_2 reduction, including the interaction of reactants with catalysts, reaction conditions, and the impact of the photoelectrode. Moreover, we compare various PEC CO_2 reduction systems, with a specific focus on enhancing the efficiency of CO_2 reduction. Finally, we provide a summary of key considering aspects for further development of the PEC CO_2 reduction.

1. Introduction

Carbon dioxide (CO_2) reduction to chemical fuels using heterogeneous catalysis is a promising approach for addressing the issues of anthropogenic CO_2 emissions and energy supply.[1–4] Several strategies such as photo-,thermo-, electro-, and biocatalysis have been utilized for converting CO_2 into products, such as CO, HCOOH, CH_4, CH_3OH, etc.[5–11] Photoelectrochemical (PEC) catalytic conversion of CO_2 into chemical fuel has shown potential for recycling CO_2 via solar energy in the past few years which can help meet our energy needs.[12–14] Solar-driven PEC CO_2 reduction possesses several key benefits such as (i) utilization of waste CO_2, (ii) useful chemicals like CO, CH_4, C_2H_6, and CH_3OH can be synthesized and (iii) it can be operated at atmospheric conditions, no harsh reaction conditions are required (compared to thermocatalysis which operates a high temperature).[15–19] Importantly, oxidation and reduction products are readily carried out in separate cells in a PEC system, which enables efficient product

separation and quantification.[13] Therefore, given the advantages of PEC CO_2 conversion, there has been growing interest from the scientific community in recent years, as shown in **Figure 1**.

The efficiency of the PEC cell depends on the light source, electrode materials, electrolyte solution, pH of the solution, bias voltage, CO_2 concentration and solubility, and the nature of the ion exchange membrane.[13,16,18] CO_2 reduction reaction includes thermodynamic and kinetic factors; the thermodynamic factors involve the photon energy and electronic band energies (i.e., valence and conduction band potentials) of the material;[20] while kinetic factors of CO_2 reduction involve charge separation, surface active sites, and adsorption/desorption of reactant/intermediates. PEC CO_2 reduction starts with charge separation when the surface of electrodes is exposed to light irradiation, followed by charge diffusion, and redox reaction in PEC cells on the surface of the catalysts.[20,21] Therefore, it is worth noting that material design plays an important role in PEC CO_2 reduction reactions. In this regard, there has been intensive investigation within the PEC and photocatalytic materials, including metal oxides,[22,23] chalcogenides,[21,24] carbon-based materials,[25,26] metal complexes,[27,28] perovskites,[29] MXenes,[30] etc. for the transformation of CO_2 into chemicals and fuels. However, single metal oxide materials such as TiO_2, WO_3, Bi_2O_3, etc. possess low light absorption ability in the visible region, poor charge separation, and insufficient active sites on the surface of the catalyst, leading to low PEC performance. Researchers have tried different approaches to enhance the usability of electrode materials and improve CO_2 conversion rates, current density, and faradaic efficiency at low bias.[31] To this end, methods like elemental doping, the use of cocatalysts, heterojunction combinations, and hybrid composites have been commonly utilized to improve the photoelectronic properties of the electrode materials.[32–35] Among these, the elemental (metal/non-metal) method is one of the

simplest and most effective strategies to enhance the photoelectronic properties of the electrode materials.[36–38]

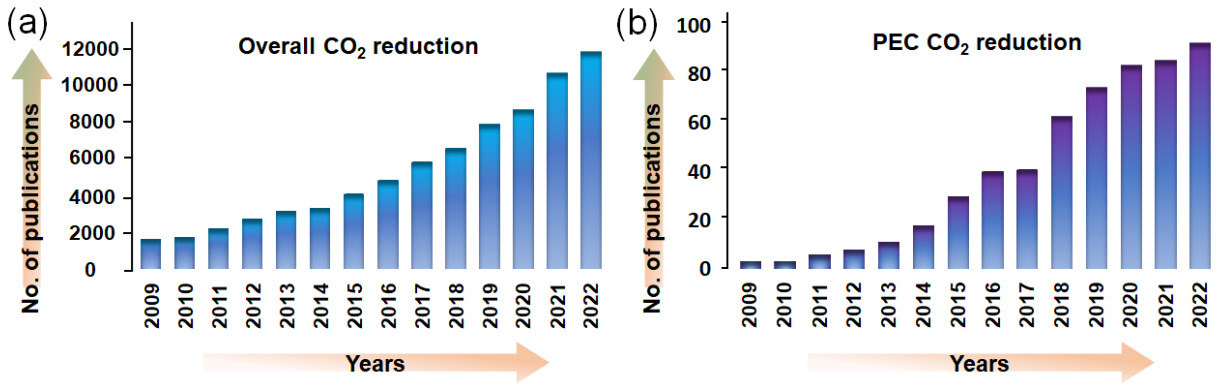

Figure 1. The publications trends on the (a) overall CO_2 reduction, and (b) PEC CO_2 reduction from 2009 to 2022, obtained from the Web of Science database using the keywords "CO_2 reduction" and "photoelectrocatalytic CO_2 reduction", respectively, with a few filters.

The elemental doping approach involves adding non-metal or metal ions to semiconductors during the synthesis of catalysts. This method has gained significant attention for various catalytic applications. When non-metal or metal ions are introduced to electrode material, it forms a defective state that changes the electronic and geometric structure of the catalysts, improving extended light absorption ability. Ran et al. demonstrated that the introduction of phosphorus (P) to g-C_3N_4 generates mid-gap states, which significantly enhances light absorption in the visible region[39]. Additionally, metal incorporation increases the local electron density of the adsorption sites on the surface of the catalyst through the interfacial charge transfer process, which enhances the electron transfer kinetics for catalysis. Jang et al. prepared N-doped ZnTe nanorods coupled with an N-doped carbon layer for the production of CO through PEC CO_2 conversion.[40] N-doping to ZnTe nanorods decreased the ZnTe's bandgap and reduced the charge recombination. Hence, enhancement in the PEC CO_2 reduction activity was observed. The surface or lattice of the

elemental doping catalyst provides numerous active sites for the absorption of CO_2 and has an impact on surface reactivity. These new active sites help stabilize the crucial intermediates of the CO_2 reduction reaction, which subsequently affects the performance and selectivity of PEC CO_2 reduction. According to the literature, the selectivity of CO_2 reaction products varies depending on the type of dopants used. The reduction of CO_2 can lead to the formation of different products through intermediates like CO_2^-, CO, COH, $HCOO^*$, CHO, etc. The selectivity of CO_2 reduction to produce specific products largely depends on the dopant's nature and the adsorption/stabilization of these intermediates. Metals like Pt, Ag, Au, and Pd tend to favor the formation of $^*CO_2^-$ intermediates that lead to CO and CH_4 products. On the other hand, In, Bi, and Sn, which have p electrons, tend to form HCOOH as the main product during CO_2 reduction through their affinity towards $^*CO_2^-$ intermediate through oxygen. Cu-based catalysts exhibit CO_2 reduction activity leading to the formation of various products such as CO, HCOOH, CH_4, CH_3OH, C_2H_4, etc. This is because of their effective binding strength with the $^*CO$ intermediate, which facilitates subsequent transformations. It has been observed that Cu^{2+} ions provide more adsorption sites for CO_2 and stabilization of $HCOO^*$ intermediate, leading to high selectivity towards formate in an aqueous solution. Gao et al. employed a Cu-doped $BiVO_4$ electrocathode for the PEC CO_2 reduction into HCOOH[41]. Non-metals such as O, S, and N can also be doped to semiconductors to form CO, CH_4, and HCOOH. For instance, Zhou et al. demonstrated the tailored product selectivity of PEC CO_2 reduction on CZTS/CdS via S-vacancy. When S-vacancies were replenished by oxygen doping (O-doping) during heat treatment in the air, CO_2 reduction towards HCOOH formation was increased. Conversely, catalyst heat treatment in an inert atmosphere promoted the desorption of surface-bound CO molecules, resulting in higher CO selectivity. Therefore, it is necessary to discuss the structure-activity relationship, which includes the doping

effect of catalysis, adjustment of bandgaps, tuning of electronic bands, charge separation, adsorption and desorption of CO_2/intermediates, and selectivity.

In our previous reviews, we explored the photocatalytic conversion of CO_2 into solar fuels.[42–46] Those included discussing the challenges involved in CO_2 photoreduction and exploring various approaches to enhancing overall activity, product selectivity, and long-term stability of CO_2 reduction reaction. There are a few review articles that provide in-depth PEC CO_2 reduction, for example, Chen et al. in 2021 summarized the fundamentals, advances, and challenges of PEC CO_2 reduction.[18] Kumaravel and coworkers published a review article on PEC CO_2 reduction emphasizing various types of materials, such as plasmonic metals, porous nanostructures carbon-based catalysts, 2D/3D materials, metal−organic frameworks, and biological molecules.[47] In another review, Tang et al. reviewed the latest developments in semiconductor-based PEC CO_2 reduction including various p-type and n-type materials.[48] Dhabarde and colleagues reviewed the preparation, characterization, and development of carbon-supported films,[21] on the other hand, Wang and colleagues reviewed Cu-based photocathodes for PEC CO_2 reduction.[49] A review by Wang and coworkers summarized the advancement in the development of CO_2 reduction through PEC reaction focusing on the electrode material design perspective.[13] The majority of review articles on PEC CO_2 reduction in the literature focus on progress and challenges, emphasizing various types of materials like p-type and n-type materials, carbon-based materials, and Cu-based photocathodes. We believe that narrowing down the topic of the review article to a specific problem and providing a comprehensive solution is crucial to deepen the understanding of the content. Therefore, in this review, we provide a detailed insight into the progress of various metal/non-metal doped electrode materials for PEC CO_2 reduction. First, insights on PEC CO_2 reduction highlighting fundamental of PEC CO_2 reduction, PEC cell, applied bias, role of electrolytes, product selectivty, kinetics and reaction mechanims were discussed. Then,

various synthesis strategies of elemental doped catalysts are disscussed. In order to emplasize the structure-activity relationship of the catalysts, the chemical composition of the material, and elemntal doping plays an important role. Therefore, the optimization strategies of the electrode materils like defect engineering, dopant-support interaction, band position alteration, introduction of active site for CO_2 adsorption, are discussed aimed at improving photoelectric properties for PEC CO_2 reduction. Later, elemental doped catalysts with activity and product selectivity of PEC CO_2 reduction, and their relationship with metal dopaning to electrode materials are disscussed. Finally, summary and outlook of the review article has been provided.

2. Fundamentals of PEC CO_2 conversion (CO_2 reduction, PEC cell, bia potential, electrolytes, reaction pathways, product selectivity)

There has been a surge in research focused on PEC CO_2 reduction in recent years to address its low activity and poor selectivity in PEC CO_2 reduction. A semiconductor photoelectrode is employed to generate electrons through photoexcitation in a PEC cell at different bias voltages. These generated electrons are then directed to the electrode surface (cathode case) by the discrepancy in energy level between the conduction band and the surface energy states and band bending at the solid/liquid interface, facilitating the catalytic reduction of CO_2, as shown in **Figure 2a**. The CO_2 molecule is linear, and to break the bond between C-O, it needs the activation energy for bond cleavage (750 kJ mol^{-1}), which can be provided photoelectrochemically in the PEC system.[50] Proton-coupled electron transfer (PCET) reaction could decrease this high required energy for CO_2 reduction.[51] Reduction of CO_2 can be carried out into different products depending on the required energy and numbers of electrons and protons, as shown in **Figure 2b**. Bias refers to the voltage or potential that is applied during the PEC CO_2 conversion process that plays a significant role on the efficiency of the CO_2 reduction reaction. It determines the driving force for

the electrochemical reduction of CO_2 and affects the kinetics of the various reaction steps. Optimizing the bias can result in improved efficiency of the reaction, leading to higher conversion rates and more selective production of desired products. For instance, Wang et al. conducted a study on the selectivity of PEC CO_2 reduction reaction using Au-loaded N-doped TiO_2 plate nanoarray photoanode and Zn-doped Cu_2O cathode to reduce CO_2 to CH_3COOH via PEC[52]. The resulting catalysts had a Faradaic efficiency of 58.1% for CH_3COOH at 0.5 V vs. Ag/AgCl, along with a small fraction of CO and H_2. Interestingly, they observed that the Faradaic efficiency of CH_3COOH decreased when the anodic potential was more positive or negative, which made C_2 selectivity dependent on the applied potential. When the bias voltage was lower than 0.5 V vs. Ag/AgCl, C-C coupling was not observed, while a higher bias voltage than 0.5 V led to the deposition of amorphous carbon that buried the catalytic active sites and inhibited the formation of CH_3COOH. Apart from that, the applied bias affects the stability of photoelectrode, an extreme bias can lead to degradation and affect performance. Therefore, optimization of bias is crucial for maintaining the PEC system's performance.

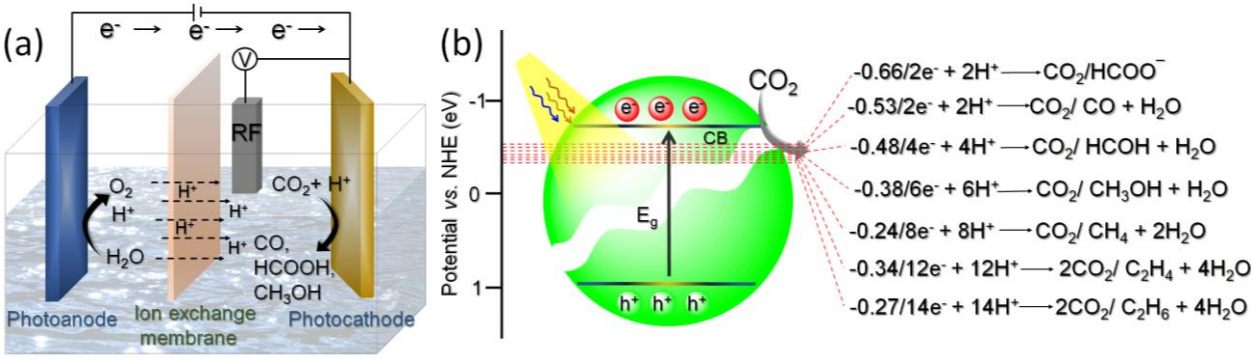

Figure 2: (a) Schematics of photoelectrochemical reduction of CO_2 in a three-electrode cell, (b) The mechanism of photoinduced CO_2 reduction into different products on a semiconductor according to their redox potentials (vs. NHE).

Besides, the electrolyte is also a key aspect in the reduction of CO_2 in PEC cells, and two main types are aqueous and nonaqueous. Aqueous electrolytes, such as bicarbonate ($NaHCO_3$, $KHCO_3$), hydroxide (NaOH, KOH), and sodium sulfate (Na_2SO_4), are used. However, due to poor CO_2 solubility in aqueous electrolytes (~34 mM under ambient conditions), nonaqueous electrolytes such as N, N-dimethylformamide (DMF), n-methyl-2-pyrrolidone (NMP), and acetonitrile (ACN) can be used.[53] Also, ionic liquids such as 1-ethyl-3-methyl-imidazolium tetrafluoroborate ([EMIM]BF_4) can be used as electrolytes.[54] According to simulation data reported by Lim et al., the overpotential energy of the first PCET step ($CO_2(g) + [H^+ + e^-] \rightarrow {}^*COOH(solv.)$) can be reduced ~310 meV in [EMIM][BF_4] and mixed solution (20:80 [EMIM][BF_4]:H_2O) compared to an aqueous solution (100% H_2O) at applied potential as −0.11 V_{SHE} on Ag(111) surface.[55] This simulation data agrees well with experimental data of Rosen et. al.'s electrochemical CO_2 conversion to CO using [EMIM][BF_4], reporting an overpotential of 0.17 V.[56] Moreover, ionic liquids have been recognized for their ability to reduce the activation energy required for CO_2 reduction and enhance the solubility of CO_2 within the electrolyte.[57] For example, Mohammed et al. reported the maximum capacity value for CO_2 of [EMIM][BF_4] was 0.0795 mol (CO_2 abs)/mol (IL).[58] Zhao et al. also measured the CO_2 solubility in 11 types of functionalized ionic liquids at room temperature and atmospheric pressure.[59] The CO_2 solubility of liquid ionic was from 0.74 to 16.2 wt.% higher than that of aqueous solution without liquid ionic (0.15 wt.%).

There are some oxygen evolution reaction (OER) photoanode cases, but most studies demonstrated p-type photocathode for the CO_2 reduction PEC systems. For p-type semiconductors, holes situated at bulk move to the interface during electrolyte contact equilibration and disclose space charge region (SCR) with fixed negative charges. The depletion layer forms by removing

the majority of holes in the SCR, resulting downward bending of the p-type semiconductor.[60,61] This downward bending at SCR occurs at the p-type semiconductor/electrolyte interface until the Fermi levels (E_f) are equal, as shown in **Figure 3**. When the negative electrical bias (E_b) is applied to a p-type semiconductor, the degree of bending can be increased. When a p-type semiconductor is illuminated and photoexcited at an equilibrium state, the as-formed electrons transfer to the conduction band while holes remain at the valence band. This induces the E_f to split into two different quasi-Fermi levels for electrons ($E_{f,n}^*$) and holes ($E_{f,h}^*$).[62] After photoexcitation, the excess electrons affect the minority carrier distribution while excess holes have little effect on major carrier distribution because the number of holes added can be negligible considering the sufficient amount of majority holes. Therefore, the quasi-fermi level of the electron shifts to the opposite compared to the initial equilibrium of E_f. The difference between $E_{f,n}^*$ and $E_{f,h}^*$ is the photovoltage (V_{ph}). The maximum photovoltage is the difference between flat-band potential (E_{FB}) and redox potential. This photovoltage effectively separates photogenerated electrons and holes. The photogenerated electrons can transfer to an electrochemical CO_2 reduction reaction due to a higher E_{CB} than the reduction potential of CO_2. However, the E_{VB} is too low to transfer the holes for oxidation reaction (O/O') thermodynamically. Therefore, the oxidation reaction happens at the anode side by applying negative bias potential to the photocathode for increasing downward band bending and lowering the counter electrode's E_F ($E_F \rightarrow E_{F'}$: not enough potential, $E_F \rightarrow E_{F''}$: enough potential for O/O'), resulting in charge separation enhancement by satisfying the electrochemical oxidation reaction (O/O').

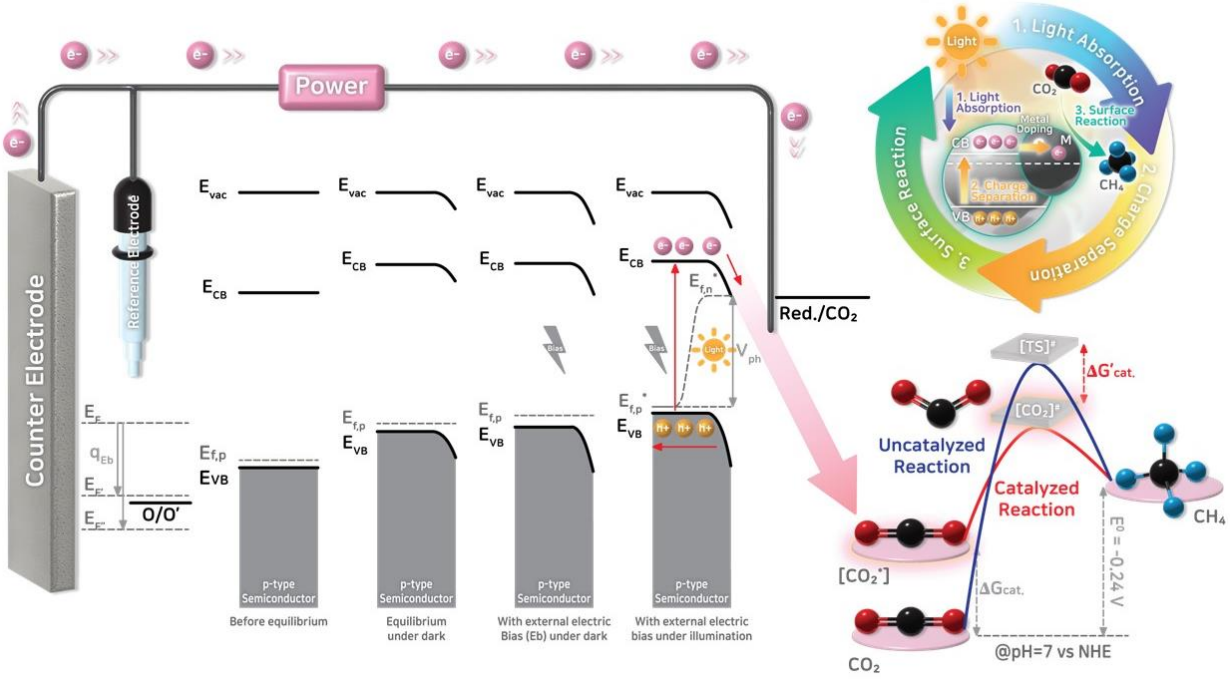

Figure 3: The band energetics of a p-type semiconductor and electrolyte contact showing the energy band diagram before & after equilibrium under dark, applied external electric bias under dark, and illumination with CO_2 activation process based on thermodynamics and kinetics. The right top Figure shows the general process of CO_2 reduction under light illumination.

To improve the charge transfer efficiency, many research groups also introduced metal doping to the semiconductor surface. Metal doping can make the trapping energy that decreases conduction band alignment as well as suppress the non-radiative recombination of charge carriers by forming spin-forbidden transition for the recombination process,[63] leading to improved charge separation and transfer. Later, the surface catalytic reaction takes place at the interface of the photocathode and electrolyte.[64] Another approach is to increase the active sites to enhance the CO_2 adsorption ability. Metal doping can lead to improved active sites for the reaction.[65–68] For example, Hu et al. theoretically predicted that the CO_2 adsorption energy of MgO significantly increased after metal (Ca, Fe, and Al) doping.[69] In another study, Cho et al. revealed that transition metal

integrated ZIF-8 ($Cu_{0.5}Zn_{0.5}$/ZIF-8) showed ~68 times higher electrochemical active surface area than ZIF-8, indicating that $Cu_{0.5}Zn_{0.5}$/ZIF-8 has more active sites for CO_2 adsorption than ZIF-8[70]. Apart from that, studies have reported that metal doping may result in faster desorption of the product resulting in high product selectivity of CO_2 reduction.[71,72] Doping can minimize the overpotential for the reduction of CO_2 by accelerating the sluggish kinetics of PCET. The well-designed catalyst can make the activated CO_2 complex ($[CO_2^*]$) and offset the activation energy of ΔG_{cat}. When electrons transfer to $[CO_2^*]$ as $[CO_2]^\#$, the energy of the transition state of CO_2 can be reduced as much as $\Delta G'_{cat}$ compared to $[TS]^\#$. These $[CO_2]^\#$ complexes undergo several steps through PCET processes to convert CO_2 into different products, as shown in **Figure 3**.[51]

The hydrogen evolution reaction (HER) is the virtually inevitable competitive reaction for CO_2 reduction reaction in the aqueous electrolyte. Low CO_2 concentration, low CO_2 flow rate, and high water content inhibit the access of CO_2 on the surface of the electrode. Also, low pH condition thermodynamically favors HER over CO_2 reduction. If the HER is suppressed effectively, various carbonaceous products of the photoelectrochemical CO_2 reduction reaction (PEC CO_2RR) can be produced depending on the type of the absorbed intermediate states (CO^*, $COOH^*$, CHO^*, and COH^*), as illustrated in **Figure 4**. The weak interaction of intermediates and the catalyst's surface leads to the formation of formate and CO. In this context, the binding nature of catalysts with reactants or intermediates significantly affects the selectivity of the CO_2 reduction reaction. For example, $CO_2^{-\cdot}$ intermediates desorb easily from the surface of In, Sn, Hg, and Pb metals, leading to produce $HCOO^-$, while Zn, Pd, Ag, Au, and Bi bind $COOH^*$ intermediates firmly but do not bind CO^* intermediates tightly leading to the formation of CO.[8] Unlike other metals, Cu can strongly bind with CO^* intermediates, generating alcohol or hydrocarbons (CH_4 and C_{2+}) via COH^* or CHO^* intermediates by dimerization process.[73] To convert CO_2 into C_{2+} products, regulation of

the microenvironment surrounding the catalytic reaction site has drawn attention dramatically due to its vital role in the reaction.[74] For example, the CO_2/H_2O ratio and pH also affect the CO_2 reduction towards C_{2+} selectivity by minimizing the conversion reaction of H_2O.

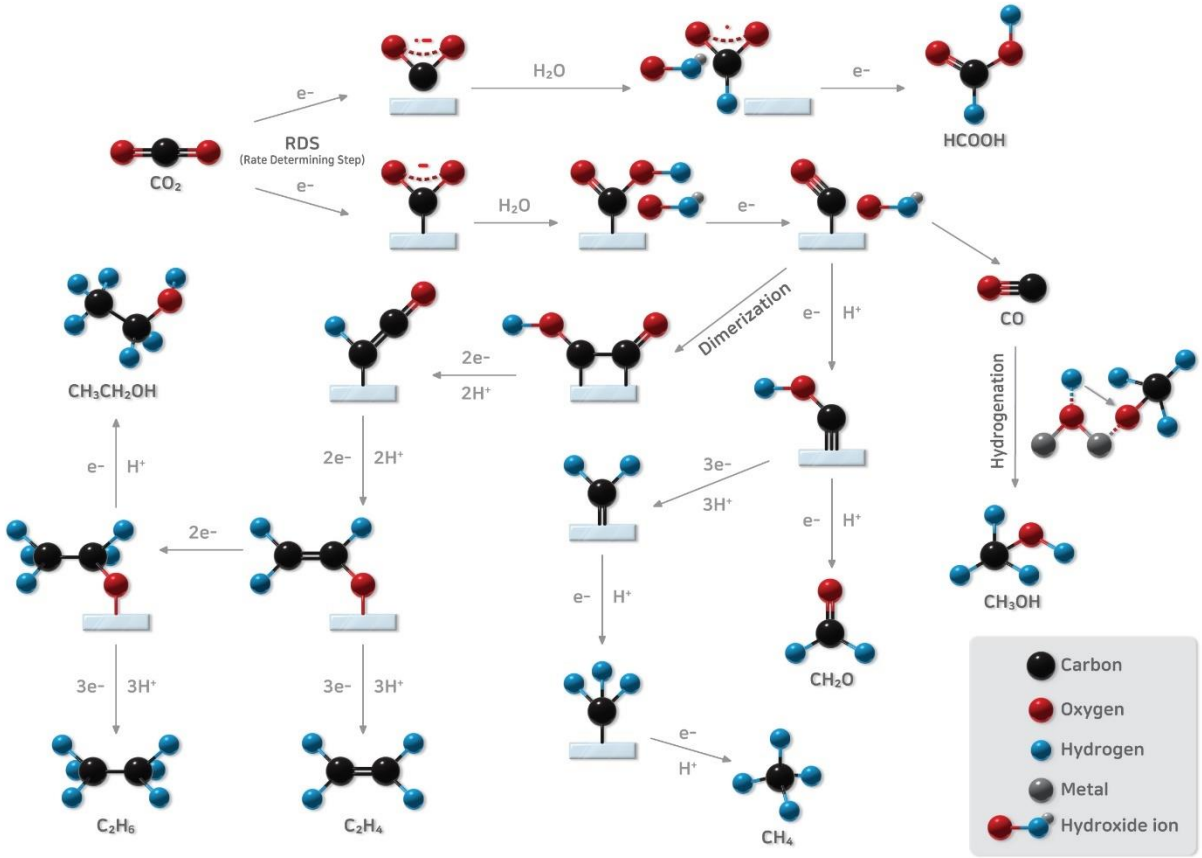

Figure 4. Schematic illustration of CO_2 reduction pathways to several products in an aqueous solution.

For example, Kim et al. developed copper (Cu) electrodes with bilayer ionomer coatings composed of the Nafion layer (Naf850) and Sustainion layer (Sus).[75] Sustainion is one of the typical anion exchange membranes (AEM) that has an affinity for CO_2 adsorption due to its imidazolium group.[76,77] Using of anion exchange membrane is also one of the HER suppression strategies however the crossover of CO_3^{2-}/HCO^{3-} and formate decreases stability[78]. In Kim et al's work, the Nafion membrane was stacked onto the sustaining membrane which traps OH^-, increasing local

pH.[75] The local CO_2/H_2O molecular ratio in the Naf850/Sus/Cu electrode is around 350 x 10^{-4} at Sus, but it is less than 100 x 10^{-4} at Naf850. This Naf850/Sus/Cu electrode displayed a C_{2+} faradaic efficiency of 90% while the faradaic efficiency for H_2 evolution was 4%, indicating that the increased CO_2 reduction activity towards C_{2+} was probably associated with the local CO_2/H_2O ratio. Also, the large cation size of the electrolyte affects C_{2+} selectivity due to the positive shift of the outer Helmholtz plane (OHP) potential of photoanode by lower hydration number of cations based on Frumkin's theory.[79,80] For example, Singh et al. measured the products of CO_2 reduction using an Ag cathode applied −1.0 V_{RHE} in a CO_2-saturated 0.1M $MHCO_3$ (M = Cs, K, Na, Li) electrolyte.[80] The faradaic efficiency of C_{2+} was 2.17 (0.1M $LiHCO_3$), 7.84 (0.1M $NaHCO_3$), 13.51 (0.1M $KHCO_3$), 36.66 (0.1M $RbHCO_3$), and 45.71% (0.1M $CsHCO_3$). Apart from the kinetics of the CO_2RR on the PEC electrodes, it has been observed that the PEC CO_2 reduction reactions possess low stability due to corrosion of the photocathode. There are two reasons for the low stability of CO_2RR. The first reason is corrosion at the photocathode. When the cathodic decomposition potential ($_nE_{decomp}$) is lower than the energy level of quasi-Fermi level for electrons ($E_{F,n}^*$), electrons can be consumed for the corrosion reaction.[81] The kinetics of the interface chemical redox reaction influences the rate of photocorrosion. In the case of a fast redox reaction on the semiconductor surface, the surface electron can be consumed, resulting in $E_{F,n}^*$ drops below the $_nE_{decomp}$. However, in the case of the slow redox reaction, the surface concentration of the electrons at the semiconductor and $E_{F,n}^*$ is affected a little, resulting in cathodic photocorrosion, and chemical redox reactions can happen simultaneously.[82] To overcome the photocorrosion issue of photocathode several strategies have been employed including (i) design of photocathode with an energy matched properly to avoid the photocorrosion reaction such as energy band alignment[83] and spatial decoupling,[84] (ii) covering the chemically unstable surface of photocathodes by

passivation layer[85] or grafting molecular catalyst,[86] and (iii) selecting a proper electrolyte with optimized pH conditions considering its electrochemical stability window in Pourbaix diagram.[87] The other reason for the low stability of CO_2RR is salt precipitation by bicarbonate formation at the cathode in the alkaline electrolyte. When CO_2 is reduced to CO at the surface of the cathode, hydroxide ions are also formed, and these hydroxide ions react with CO_2 molecules, forming carbonate ions (CO_3^{2-}). Cations from electrolytes such as K^+ can be migrated to the surface of the cathode by the electric field. These cations and CO_3^{2-} can induce salt growth at the surface of the cathode This carbonate salt can be removed by (i) reducing cation concentration, (ii) flushing water to the cathode, (iii) pulsed electrolysis, and (iv) using a bipolar membrane.[88] (i)-(iii) techniques decrease the concentration of carbonate ions at the surface of the cathode by mechanical force or methods. Especially for reducing metal cation concentration, there is a exchange between salt formation and cell voltage drop. Endrődi et. al. measured the CO_2 reduction performance with 0.1M KOH and pure water electrolyte using MEA applied 3.1 V_{cell}.[89] The current density with 0.1M KOH was 300 mA cm^{-2}, but that with pure water decreased to 100 mA cm^{-2}. Also, the charge transfer resistance (R_{ct}) value increased 3 times approximately when they changed the electrolyte from 0.1M KOH to pure water, due to the low ionic conductivity of the electrolyte. CO_2 electrolyzer using pure water exhibited high stability over 100 h operation with the faradaic efficiency of CO (FE_{CO}) staying 90-95%.[90] Zhao et al. also reviewed a study on CO_2 electrolyzers using pure water compared to various electrolytes.[91] They reported that a CO_2 electrolyzer using pure water showed higher stability (over 200 h, FE_{CO}: 70-85%) than a CO_2 electrolyzer using other electrolytes such as alkaline for producing C_1 product (over 20 h, FE_{CO}: over 99%).[89,92] It means that avoiding an excess amount of cation is beneficial for stability but a small amount of cation is essential for ionic conductivity. Therefore, flushing water and using pulsed electrolysis are alternatives to reduce the concentration of

cations at the surface of the cathode temporarily. The bipolar membrane consists of two types of membranes, (i) the cation exchange membrane (CEM) which is situated at the cathode, and (ii) an anion exchange membrane (AEM) which is situated at the anode. The water inside the bipolar membrane is separated into protons (H^+) on the cathode side and hydroxide ions (OH^-) on the anode side. These protons from CEM interact with bicarbonate to regenerate CO_2. Also, the metal cation migration is decreased then the proton turns into the primary charge carrier. Therefore, the migration of lots of metal cations is reduced, resulting in metal cation carbonate precipitation decreases.

3. Synthesis methods for elemental doped catalysts

The synthesis of photoelectrode materials with high catalytic active sites, through the incorporation of elemental-doped catalysts, is feasible using a range of synthesis techniques discussed below.

3.1 Sol-gel method

Sol-gel is a commonly used chemical method for elemental doping to semiconductors from a colloidal suspension wherein a dopant can be introduced by adding an aqueous solution of a metallic salt[93][94]. Usually, it involves the formation of sol by mixing the catalyst precursor with solvents which further undergo hydrolysis and condensation reactions and the different processes that affect the precursor to form a fluid with viscosity known as a gel. Then it is subjected to the calcination for metal/non-metal ion doping of semiconductors. A broad range of metal oxides and their composites have been reported in the literature for the synthesis of catalysts for CO_2 reduction applications using the sol-gel route[95][96]. It has several advantages including an easy synthesis procedure, the use of mild reaction conditions, and a scalable technique. In-situ fabrication of the elemental doped materials on photoelectrode can be achieved by sol-gel technique, for example, hydrothermal-assisted sol-gel and microwave-assisted sol-gel are sub-categories of the sol-gel synthesis used in various catalytic materials. For example, Benammar et al. prepared rare earth elemental (such as Er and Yb) doped

Y2Ti2O7 pyrochlore NPs by using the hydrothermal-assisted-sol-gel method[97]. This method leads to control structure and morphology of the materials, which makes it possible to prepare tailor-made material for specific applications. In another study, Gorli et al. prepare Zr-doped TiO_2 photocatalysts using a microwave-assisted sol-gel approach which facilitates the substitutional doping of Ti^{4+} with Zr^{4+}, resulting in reducing the band gap and high efficiency in the segregation of photogenerated charge carriers for catalysis[98]. Their research emphasized that a microwave-irradiation method has various advantages over traditional heating, such as easy, and fast synthesis, and high thermal homogeneity can be achieved, which will assist in lowering calcination temperatures.

3.2 Electrochemical process

The electrochemical process employs a three-electrode setup in an electrolyte solution to deposit specific materials onto a desired substrate[99]. Through this approach, it is possible to design and synthesize metal-doped semiconductors, which can be tailored to modify the localized electronic structure, making them suitable for PEC CO_2 reduction[100]. The synthesis rate can be precisely regulated by adjusting both the applied voltage and the physicochemical properties of the electrolyte. Several studies employed this method for the preparation of photocathodes for PEC CO_2 reduction[101–104]. For example, Guo et al. developed a PEC CO_2 reduction system by electrochemically depositing gadolinium (Ga) doped Cu_2O onto a Cu mesh[105]. The synthesis involved mixing $CuSO_4 \cdot 5H_2O$ and 2-hydroxy propionic acid, adjusting the solution pH to 11 with NaOH, and electrodeposition at -0.6 V bias voltage for 30 min at 60 °C. A standard three-electrode cell system was used with the Cu mesh as the working electrode, Pt electrode as the counter electrode, and Ag/AgCl electrode as the reference electrode. After deposition, the material was washed, vacuum-dried at 50 °C, and subjected to thermal treatment at 600 °C in N_2 for 3 h to obtain the catalyst (Ga-Cu_2O). For the synthesis of catalysts, the morphology and structure of the catalysts in the

electrochemical technique can be influenced by various factors such as electrolyte solution, pH, overpotential, and substrate type, therefore the optimization of these parameters is necessary to obtain the ideal catalysts[99].

3.3 Hydrothermal treatment

The hydrothermal technique is well known for synthesizing various materials within a sealed reactor, utilizing an aqueous solution at elevated pressure and temperature. The conditions of high temperature and pressure in the reactor facilitate the synthesis of highly crystalline materials. The hydrothermal method allows for the synthesis of materials with diverse compositions, including elemental doping, heterostructures, binary or ternary composite structures, etc. for various applications. For example, Yan et al. employed a hydrothermal method for the synthesis of Sb-doped SnS_2 used for electrochemical CO_2 reduction to formate[106]. Similarly, it has been one of the commonly utilized methods for the fabrication of photocathode materials for PEC CO_2 reduction[41,107,108]. Li et al. prepared Bi, and S codoped SnO_x catalysts through a hydrothermal method for PEC CO_2 reduction[109]. Briefly, a precursor (i.e., $SnCl_4 \cdot 5H_2O$) was mixed with dopants such as $Bi(NO_3)_3$ and thiourea in distilled water. Then, the mixture was then transferred to a Teflon-lined stainless steel autoclave and reacted at 160°C for 6 hours. After cooling, the sediment was collected, washed, and dried. The obtained powder was calcined at 400°C for 2 hours to get the desired catalyst for the PEC CO_2 reduction reaction.

3.4 Thermal treatment

In this method for synthesizing catalytic materials, heat is employed to decompose chemical bonds within the compound. This process allows the formation of monodispersed NPs with varying sizes, depending upon the reaction conditions. As this technique relies on high temperatures for catalyst

synthesis, the thermal energy induces the elemental doping to support the material and the creation of defect states, thereby modifying the optoelectronic properties of the materials for CO_2 reduction[110]. Lu and colleagues synthesized Re (Rhenium)-doped CuO NPs supported on TiO_2 NTs for PEC conversion of CO_2 to alcohols through thermal decomposition[111]. In this process, the Re precursor, i.e., ammonium perrhenate (NH_4ReO_4) was introduced into a solution of copper nitrate. The resulting solution was then coated onto the TiO_2-NTs support under vacuum conditions. Various calcination temperatures were employed during the fabrication of Re-doped CuO supported catalysts. In another study, Wang et al. introduced a thermal polymerization technique for the synthesis of O-incorporated C_3N_4 NSs which was employed for PEC CO_2 reduction[112]. The thermal decomposition technique has a limitation due to its dependence on high temperatures, and the determination of processing parameters can be a time-consuming aspect.

4. Elemental doped photoelectrodes: effect of doping on PEC CO_2 reduction

To achieve the feasible CO_2 conversion, the energy level of the conduction band should be above the CO_2 reduction potential to specific products (e.g., −0.61 V vs. NHE for CO_2/HCOOH) while the valance band potential should be below H_2O/O_2 oxidation (i.e., 0.82 V vs. NHE), respectively. Suitable catalysts are essential for the PEC CO_2 conversion process to achieve high efficiency. Single semiconductor materials, for instance, TiO_2, ZnO, SnO_2, and C_3N_4 are commonly used materials for PEC reactions that possess a wide band gap that can produce a high photovoltage; however, it leads to limited light absorption of the visible light region as well as charge recombination. In the context of efficient CO_2 conversion, non-metal or metal doping can alter the optoelectronic properties of support. Introducing impurities into the crystal lattice of support materials creates surface defects and modifies the electronic band structure, which increases light absorption across a wide range of the spectrum and enhances charge separation ability. Dopants also serve as CO_2 adsorption sites, which

effectively improve CO_2 adsorption, resulting in improved catalytic activity and high product selectivity. **Figure 5** illustrates the concept of elemental doping to photoelectrodes and its impact on PEC CO_2 reduction.

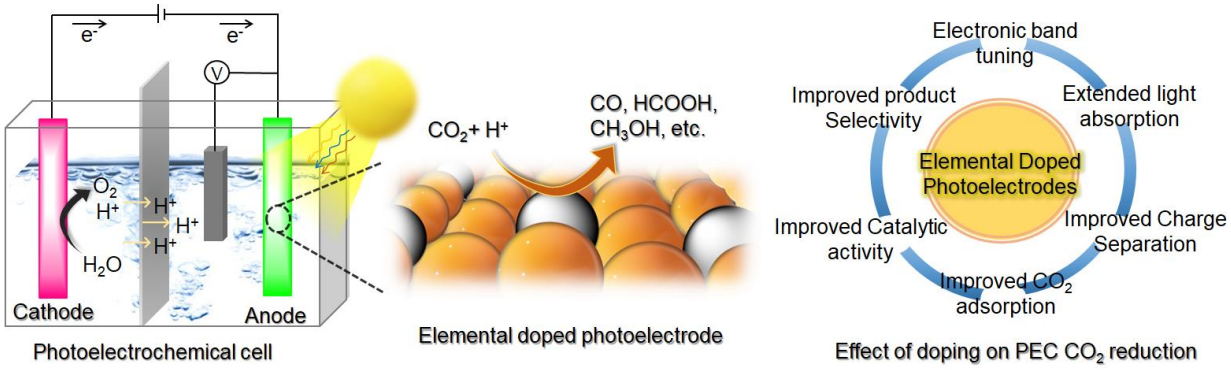

Figure 5: Schematic representation of the effect of elemental doping on PEC CO_2 reduction**.**

4.1 Non-metal doped photoelectrodes

Studies have been reported on non-metallic heteroatom doping in semiconductor materials, including N, O, B, S, etc. Non-metal doping improves the optoelectronic properties of the semiconductor and creates active sites for CO_2 reduction. For example, Wang et al. introduced the effect of O-doping on the C_3N_4 photoanode used for PEC CO_2 reduction that significantly improved photoelectric efficiency towards formate formation as compared to pristine C_3N_4z In this study, four different samples of C_3N_4 (referred to as CN1, CN2, CN3, and CN4) were prepared with different oxygen contents using thermal polymerization. CN1 was synthesized by mixing melamine and urea (oxygen-containing precursor), then heating under N_2 flow while CN2 was prepared under N_2/O_2. CN3 was obtained by heating melamine without mixing urea under N_2, and CN4 was prepared using the same process as CN3, but thermally polymerized under N_2/O_2. The electrical conductivities and photoelectric responses of CN1 were improved by incorporating controlled oxygen content, doping form, and surface defects, leading to better separation of photo-generated charges during PEC CO_2

reduction. According to the photocurrent response (**Figure 6a**), the CN4 sample, which was synthesized by pyrolysis of melamine in an inert atmosphere (i.e., N_2), possessed the lowest photocurrent response under light irradiation. While the CN1 sample synthesized using the oxygen-containing precursor (ie., urea) demonstrated the highest photocurrent response among all samples, this suggests that oxygen is useful for the separation of charges. Therefore, the CN1 catalyst showed higher PEC CO_2 reduction to formate activity with a rate of 273.58 μmol cm^{-2} h^{-1} at a bias of −0.9 V vs. RHE (**Figure 6b-c**) as compared to the other samples. It also demonstrated remarkable stability in photocurrent density during 24 hours of exposure to light. As it is widely recognized, the process of CO_2 reduction to produce value-added chemicals is intricate, involving various pathways and the formation of multiple intermediates such as CO^*, COH^*, and CHO^*

Efficient charge carrier transfer improves the PEC CO_2 reduction catalytic activity, whereas the photocathode's surface states regulate the product selectivity. Therefore, adsorption and desorption of products/intermediates tune the selectivity of CO_2 reduction towards specific products. Usually, defect states (such as vacancies) are produced by eliminating/replacing atoms from semiconductor lattices; these defects serve as catalytic active sites for CO_2 reduction reactions. Therefore, tuning surface defect states is one of the efficient strategies for altering the CO_2 reduction reaction pathway that tunes the product selectivity. In this regard, recent research by Pang et al. demonstrated very meaningful results.[113] They found that creating S-vacancies in ZnS by Ni-doping dramatically increases the activity and selectivity toward photocatalytic CO_2 reduction to HCOOH. Zhou and colleagues also accelerated electron transfer and altered product selectivity on CZTS/CdS by introducing the S-vacancies for PEC CO_2 reduction.[114] The CZTS/CdS catalyst underwent a synthesis process involving heat treatment in distinct environments, specifically air, and N_2, as shown in **Figure 6d**.

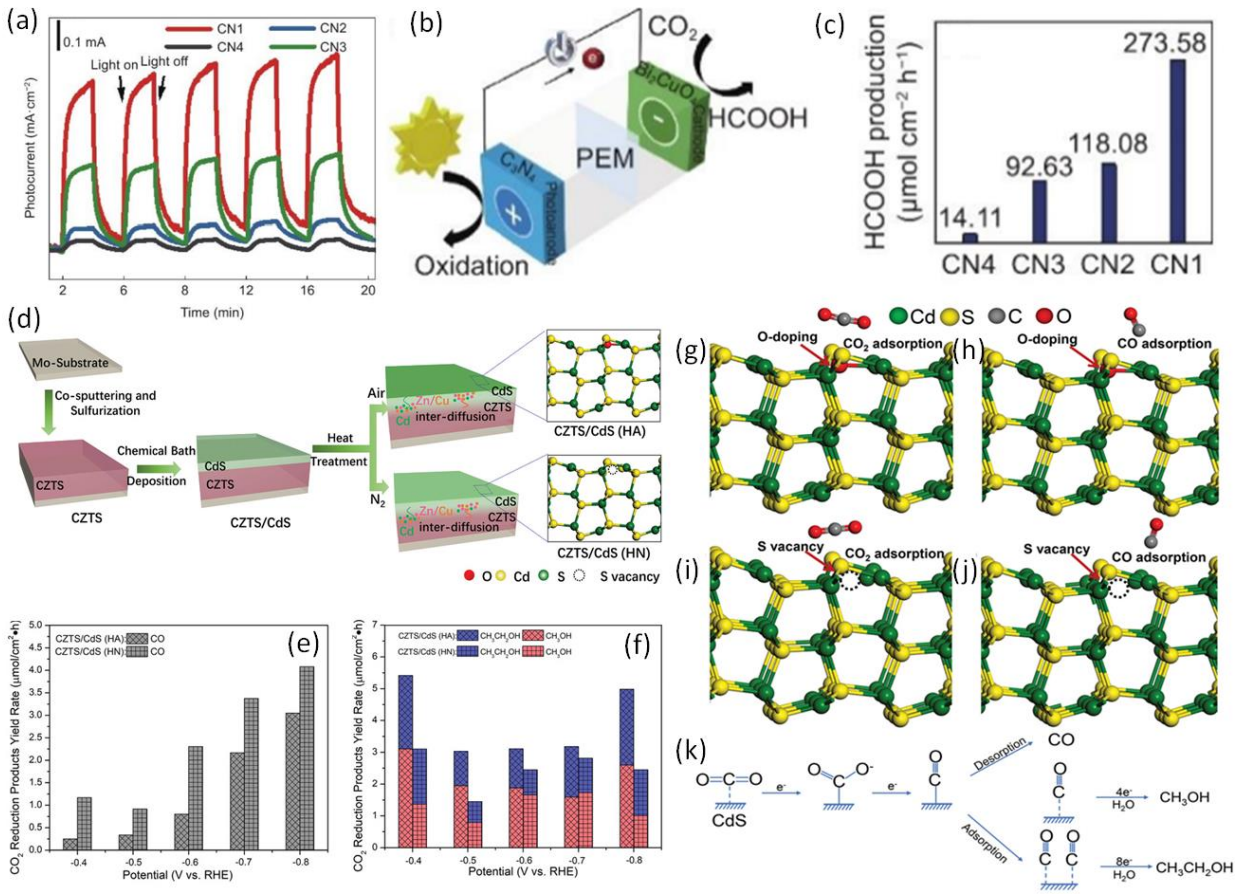

Figure 6: (a) Transient amperometric I-t curves at -0.9 V vs. RHE under 1.5G illumination, (b) schematic illustration of PEC CO_2 reduction in CN photoanode and (c) PEC performance of CN toward CO_2 reduction to formate. Taken with permission from ref.[112]. Copyright 2022, Elsevier Publications. (d) Synthesis process of various samples of CZTS, (e) CO_2 reduction to CO, and (f) hydrocarbons in CZTS/CdS (heat treatment in the air (HA)) and CZTS/CdS (heat treatment under N_2(HN), DFT optimized structures for CO_2 and CO absorbed on (g-h) O-doped CdS and (i-j) CdS with S-vacancy, and (k) CO_2 reduction pathways to CO and hydrocarbons. Taken with permission from[114], Copyright 2021, Wiley Publications.

This process resulted in a deliberate alteration of surface vacancies on the CdS component. When CZTS was subjected to heat treatment in an air atmosphere, S-vacancies were refilled by O-

doping. This modification effectively adjusted the catalyst's capacity for adsorbing CO_2 and CO, thus enhancing its selectivity towards hydrocarbon formation during CO_2 reduction (**Figure 6e**). Conversely, when the catalyst underwent heating in an inert condition (i.e., N_2), it led to an increased presence of S-vacancies on the catalyst's surface. This, in turn, promoted the desorption of surface-bound CO molecules, resulting in higher CO selectivity, as shown in **Figure 6f**. Based on DFT calculations, it is observed that the introduction of oxygen (O) into CdS enhances its ability for CO_2 adsorption. However, the adsorption energy for CO is comparatively lower on O-CdS, consequently, strong adsorption of CO_2 molecules was observed on the surface of the catalyst, which in turn promotes the generation of higher hydrocarbons, as depicted in **Figure 6g-h and k**. Conversely, when CdS lacks O-doping (i.e., S-defected CdS), its adsorption energy for CO is higher, resulting in enhanced CO desorption capacity. Consequently, this configuration tends to favor the production of CO as the primary product in CO_2 reduction, as depicted in **Figures 6i-j and k**.

In vise-versa of the previous example, sulfur (S) was employed as a dopant to the Cu_2O/CuO hybrid structure to achieve an increased PEC CO_2 reduction.[104] In this study, the band gaps for Cu_2O/CuO and S-Cu_2O/CuO were observed as ~1.92 and ~2.05 eV, correspondingly. Electronic delocalization occurs in the S-Cu_2O/CuO cluster as a result of sulfide bridges present in the inner layer of the surface of the catalyst. CO_2 conversion to methanol and acetone is driven by the generation of H^+ on the counter electrode, as shown in **Figure 7a**. A slight increase in the band gap (~0.15 ev) after S-doping to Cu_2O/CuO endorses the conduction band from 0.43 to 0.46 eV vs. RHE which was reported to decrease electron-hole recombination for CH_3OH and CH_3COCH_3 formation. Thus, improved PEC CO_2 reduction under light illumination was achieved from the S-Cu_2O/CuO for the CH_3OH and CH_3COCH_3 formation with the rate of 32 μmol cm^{-2} h^{-1} and 22

μmol cm^{-2} h^{-1}, respectively. The cumulative Faradaic efficiency of 75% was obtained at a low overpotential of 0.47 V vs. RHE. Importantly, the photocurrent density of the S-Cu_2O/CuO was -0.34 mA cm^{-2}, which was 118 times higher as compared to Cu disc and 2.5 times higher than Cu_2O/CuO with excellent photocurrent stability of ~8000 s. Overall, doped sulfur acts as an electron transfer mediator in Cu_2O/CuO structure, tunes the energy band position, and promotes electron mobility by O-vacancy formation to improve the catalytic activity and photocurrent stability of PEC CO_2 reduction. During PEC CO_2 reduction, electrode materials can undergo photoelectrochemical corrosion in aqueous electrolyte solutions that can limit the stability of the reaction. To address the stability and photocorrosion issue, elemental doping can be applied to the electrode material. Jang and colleagues synthesized N-doped ZnTe nanorods adorned with an N-doped carbon layer using an entirely solution-based method. This approach facilitated the selective PEC conversion of CO_2 to CO at an applied bias of −0.11 V vs. RHE.[40] Incorporating N-doping into the nanorods of the ZnTe lattice results in a reduction of the catalyst's bandgap and an enhancement of the charge transfer capability, ultimately improving the activity and stability of the reaction, as illustrated in **Figure 7b-d**. The faradaic efficiency of N-doped ZnTe was ~80%. However, the application of an N-doped carbon layer on ZnTe nanorods significantly improved faradaic efficiency exceeding 90%. The improved faradaic efficiency was ascribed to the diminished photocorrosion and increased catalytic stability observed in an aqueous electrolyte solution. Additionally, the high conductivity of the carbon layer facilitates efficient charge transfer. The N-doped carbon, with its lone-pair electrons, promotes the adsorption and activation of CO_2, leading to selective production of CO on the catalyst's surface through PEC CO_2 reduction.

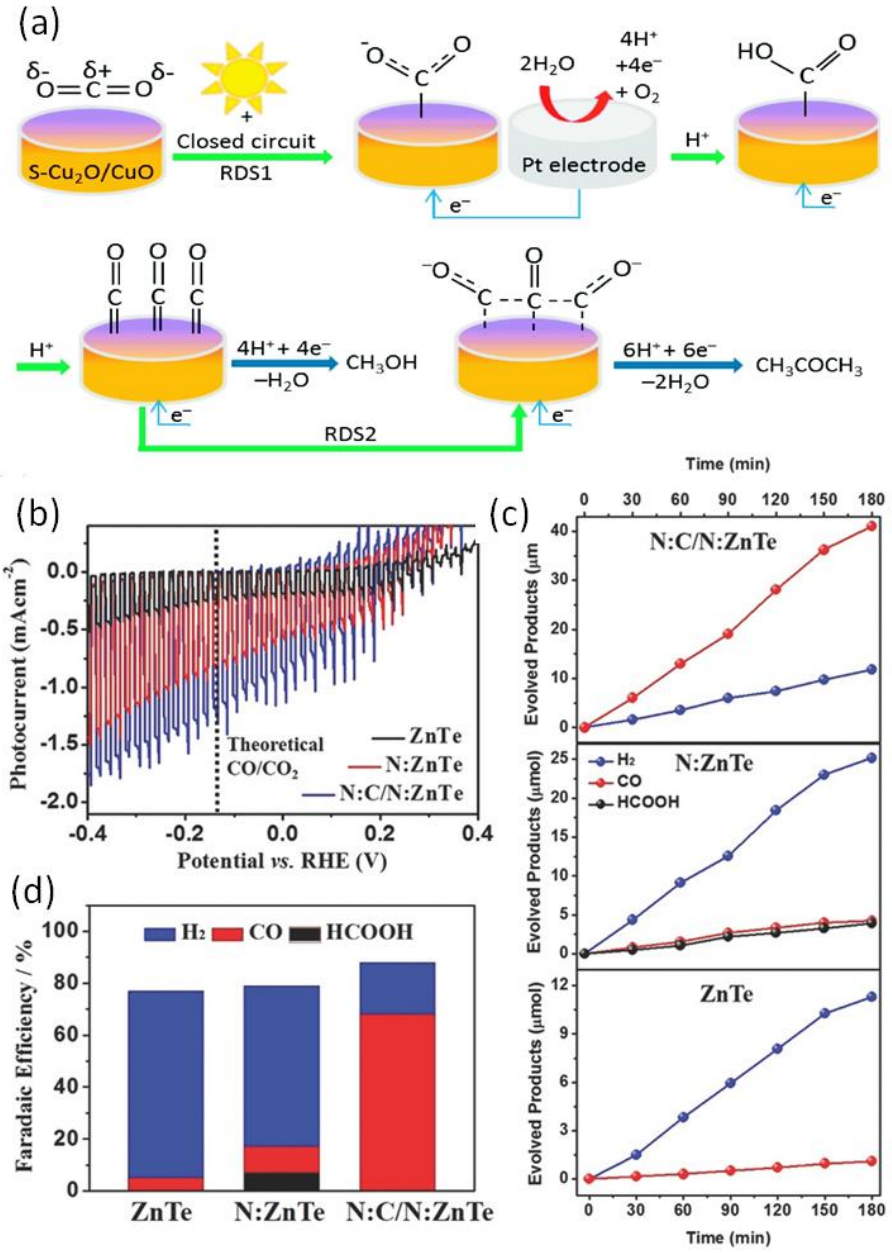

Figure 7: (a) CO_2 reduction mechanism to CH_3COCH_3 using S-Cu_2O/CuO, Taken with permission from[104], Copyright 2017, Elsevier. (b) *J–V* curves, (c) PEC CO_2 reduction to products, and (d) Faradaic efficiencies of the evolved products for N:C/N: ZnTe samples. Taken with permission from[40], Copyright 2018, Wiley Publications.

In a previous example, non-metal doped electrode materials have been discussed for PEC CO_2 reduction, while literature also reported the combination of non-metal elements doping and introducing metal NPs cocatalysts together to the semiconductor to promote PEC CO_2 reduction more efficiently. For example, Sagara and coworkers reported a p-type boron (B)-doped g-C_3N_4 coated with Au, Ag, or Rh cocatalyst that showed significantly improved PEC CO_2 reduction activity towards C_2H_5OH formation.[110] The electronic band structure of g-C_3N_4 was modified through optimal doping of B to create BCN. As a result, the VB and CB were situated at +2.19V and −0.44V vs. NHE at pH 0, respectively. The p-type characteristics of BCN make it effective for CO_2 reduction, with its high CB potential allowing it to produce various CO_2 reduction products. This led to a significant increase in photocurrent response, with BCN exhibiting a response about fivefold more than pristine g-C_3N_4. Furthermore, the introduction of Au, Ag, or Rh cocatalysts to B-doped CN improved its catalytic activity. All the samples showed CO_2 conversion activity towards C_2H_5OH as a major product with a small amount of CO. Among them, B-doped CN with Au coating (Au-BCN) showed the highest CO_2 reduction activity towards C_2H_5OH with a rate of 150 nmol than pristine CN (~60 nmol), Ag-BCN (~60 nmol) and Rh-BCN (~100 nmol). The enhanced catalytic activity of Au-BCN in converting PEC CO_2 to C_2H_5OH resulted from improved charge separation. While multi-electron reduction of CO_2 facilitated by metal particle electron accumulation increased C_2H_5OH selectivity. In another study, a photoanode made of Au-loaded N-doped TiO_2, and a dark cathode made of Zn-doped Cu_2O were used to reduce CO_2.[52] The results demonstrate that Zn-doped Cu_2O was one of the important factors in modifying the electronic structure and active site of Cu to promote $^*CH_2$/$^*CH_3$ intermediates formation/stabilization for C-C coupling to produce CH_3COOH.

Yupeng et al. modified SnO_2 by Bi and S co-doping to improve the photoresponse towards CO_2 reduction to formate.[109] SnO_2 has a wide band gap, making it challenging to be excited by

visible light. The pristine SnO_2 has a polygon structure of ~10 nm in size, with interplanar distances of 0.247 nm and 0.325 nm, corresponding to the (110) and (101) planes. Bi^{3+} and S^{2-} doping to SnO_2 causes decreased interplanar distances to 0.241 nm and 0.325 nm for (110) and (101) planes, respectively. Therefore, introducing Bi^{3+} and S^{2-} doping into the lattice structure of SnO_2 severally replaces Sn^{4+} and O^{2-} respectively, which narrows the bandgap and enhances its optoelectronic properties. The doped 3%-(Bi, S)-SnO_2 exhibited a formate faradaic efficiency of 55.6% at a low overpotential of around 360 mV and a current density of 9.33 mA cm^{-2} at −1.4 V vs. Ag/AgCl. Enhanced catalytic activity was due to the lattice defect caused by elemental doping to SnO_2 and increased catalytic reactive sites for CO_2 adsorption/activation.

4.2 Metal-doped photoelectrodes

The introduction of transition metals as dopants in semiconductors induces alterations in the crystal structure and the generation of novel active sites, resulting in enhanced CO_2 reduction activity. Moreover, transition metals with their multi-valency, improve charge separation and transfer by trapping photogenerated electrons and holes leading to enhanced catalytic activity.[115,116] Nevertheless, excess doping acts as recombination centers and may reduce the photocatalytic activity.[117] Cobalt (Co)-doped MoS_2 catalyst was prepared to achieve PEC CO_2 reduction to methanol formation.[118] Co is an inexpensive and non-toxic element. The introduction of Co-doping into MoS_2 results in the formation of new active sites which lowers the conductive band, narrows the band gap, and enhances the charge separation for the reduction of CO_2 induced by solar light. In this study, Co-doped MoS_2 exhibited suitable band positions for CO_2 reduction, where their VB and CB were situated at 0.89 V and −0.52 V, respectively. According to EIS (electrochemical impedance spectroscopy) results, the conductivity was significantly increased after Co-doping to MoS_2. The importance of the PEC system has also been investigated. The CO_2 conversion to

methanol using Co-MoS_2 NPs was 35 mmol L^{-1} in 350 minutes, which was higher than that of photocatalysis (i.e., 7 mmol L^{-1}), electricity (i.e., 8 mmol L^{-1}), and combined photo and electricity (i.e., 18 mmol L^{-1}), as shown in **Figure 8a**. The Co-doped MoS_2 NPs' electronic band potentials are sufficiently oxidative to facilitate the H_2O oxidation reaction and produce hydrogen proton, and the conduction band is also suitable for CO_2/CH_3OH reduction potential, as shown in **Figure 8b**. Apart from that, researchers utilized Co doped CdS QDs as a superior photocathode in combination with p-nCu_2O loaded FeOOH in a recent study[119]. The resulting composite photocathode, which is known as FeOOH/p-nCu_2O/Co:CdS, demonstrated an improved photovoltage and produced HCOOH with a selectivity of faradaic efficiency of 82.9%. The addition of Co impurities to CdS helped to decrease the band gap of the photocathode, thus improving its light absorption in the visible range and increasing its photoelectrochemical properties. The study revealed that the outer layer of the photocathode, made up of Co doped CdS, increased the binding energy toward the *OOCH intermediate, resulting in the formation of HCOOH with high selectivity.

Surface Cu^{n+} sites in Cu-based catalysts have been proposed as active sites for CO_2 reduction.[120] When Cu is added to metal oxides (e.g., TiO_2), it can replace titanium atoms in the crystal lattice and create a vacancy state beneath the TiO_2 conduction band. This process introduces a new energy level to increase the light response of TiO_2 in the visible region. In this regard, Hasan et. al. prepared a Cu-doped RGO-TiO_2 nanocomposite for the reduction of CO_2 into higher hydrocarbon products such as formic acid and methanol.[121] The Cu-doped RGO-TiO_2 exhibits enhanced light absorption in the visible region (400-800 nm) than TiO_2 and RGO-TiO_2 samples. The addition of Cu to the TiO_2 lattice offers intermediary states for the transportation of photogenerated electrons, facilitating the successful electron-hole pairs separation. Consequently,

the catalyst underwent CO_2 photoelectrocatalysis under light irradiation, resulting in a photocurrent density of 1.31 mA cm^{-2} at -0.61 V vs. SCE with HCOOH (255 mmol h^{-1} cm^{-2}) and CH_3OH (189.06 mmol h^{-1} cm^{-2}) were generated during the photoelectrochemical CO_2 conversion process in methyl diethanolamine solution. At first, HCOOH was formed, serving as an intermediate in the subsequent formation of CH_3OH. However, after 3 hours of reaction time, the production of CH_3OH was increased in the Cu-RGO-TiO_2.

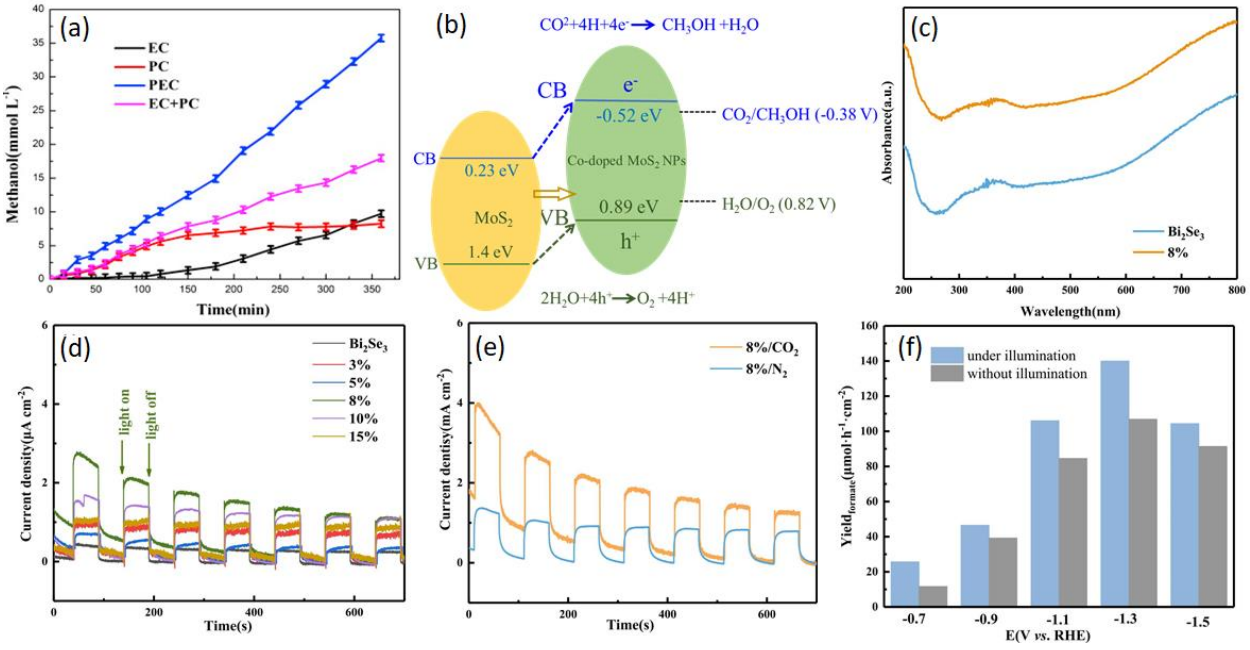

Figure 8: (a) CO_2 reduction to methanol in different catalysis conditions using Co-doped MoS_2 NPs, (b) PEC CO_2 reduction mechanism on the Co-doped MoS_2. Taken with permission from[118], copyright 2015, Elsevier. (c) UV–Vis spectra of Bi_2Se_3 and 8% Cu-Bi_2Se_3, Photocurrent response (d) with different doping ratios of Cu atoms to Bi_2Se_3, (e) 8% Cu-Bi_2Se_3 in CO_2 and N_2 atmosphere, and (f) formate yield in 8% Cu-Bi_2Se_3 for PEC and EC systems. Taken with permission from[107], Copyright 2022, Elsevier.

In another study, Zhu and colleagues developed a Cu-doped Bi_2Se_3 catalyst that generates selenium (Se)-vacancies through the oxidation state mismatch of cations which promotes CO_2

adsorption and enhances the catalytic activity for PEC CO_2 reduction into formate.[107] UV-Vis spectra showed that an 8% Cu-doped Bi_2Se_3 has improved light absorption in the visible range as depicted in **Figure 8c**. Optimum Cu-doping to Bi_2Se_3 significantly enhanced photocurrent response in the CO_2 atmosphere, see **Figure 8d-e**. The faradaic efficiency of Cu-Bi_2Se_3 was achieved to be 65.31% for formate with a negative potential of −1.3 V vs. RHE which was three times higher than pristine Bi_2Se_3. Furthermore, CO_2 reduction through a photoelectrochemical system under solar light yielded 139.97 μmol h^{-1} cm^{-2} of formate, as shown in **Figure 8f**.

In another study, Cu-doped $BiVO_4$ was also reported for PEC CO_2 reduction towards HCOOH formation where Cu^{2+} ions in $BiVO_4$ provide abundant active sites for the adsorption and activation of CO_2.[41] Cu addition to $BiVO_4$ reduces interfacial charge separation resistance and increases the charge transfer and surface reaction rates, as shown in **Figure 9a**. Hence, the optimized sample of Cu- $BiVO_4$ showed high selective electroreduction of CO_2 towards formate formation with a faradaic efficiency of 87.15 % at −1.0 V vs. RHE **(Figure 9b & c)**. In the context of CO_2 reduction through PEC, the combination of Cu-$BiVO_4$ and WO_3 resulted in the generation of formate at a rate of 354.26 μmol h^{-1} cm^{-2} when operated at −1.2 V vs. RHE, as shown in **Figure 9d**. Moreover, the Cu-doped $BiVO_4$ cathode showed excellent stability (~24 h at −1.0 V vs. RHE) and the faradaic efficiency was also stable between 86.5-93%. Apart from the above-mentioned band energy and defect engineering approaches, Zhang and colleagues introduced a hydrophilic-hydrophobic structure of Cu-SnO_2/ZIF-8 composite compounding ZIF-8 with hydrophobic and Cu-SnO_2 with hydrophilic characteristics.[122] Usually, the limited solubility of CO_2 in the aqueous phase, and competition of the HER, results in low activity of CO_2 reduction. When H_2O is used as a proton source, catalysts utilize a small quantity of CO_2 dissolved in water, precluding the use of gas-phase CO_2 for the reaction. The hydrophilic-hydrophobic structural approach proves beneficial

in augmenting CO_2 reduction by restraining HER. The hydrophobic layer facilitates the direct transport of CO_2 gas to the reaction system, thereby suppressing the competitive HER. Meanwhile, the hydrophilic layer contributes protons to the reaction, effectively enhancing CO_2 reduction. Herein, the ZIF-8 structure promoted electron transfer while Cu-doped SnO_2 provided additional active sites for CO_2 adsorption to promote the PEC CO_2 reduction towards HCOOH formation. Moreover, the porous structure of ZIF-8 enhanced the adsorption of CO_2, and its hydrophobic nature enables the capture of CO_2 bubbles directly in the electrolyte, allowing for the coexistence of gas, liquid, and solid phases at the nanometer level. This structure facilitates the CO_2 transfer from the gas phase to the PEC reaction interface, resulting in the efficient capture of electrons and improved photoelectric catalytic efficiency. Cu ions impurity introduced to SnO_2 improved visible light absorption and inhibited the recombination of electrons and holes. The Cu-SnO_2/ZIF-8 composite exhibited enhanced photocatalytic and electrocatalytic properties (faradaic efficiency: 68.96% for HCOOH, an overpotential: ~364 mV, and current density: 12.8 mA cm^{-2} at −1.4 V vs. Ag/AgCl). In another study, Yang and colleagues conducted a study on Cu and N-doped SnO_2 for effective photoelectrochemical conversion of CO_2 to formate.[108] The findings showed that the introduction of Cu and N to SnO_2 greatly improved the catalytic activity for CO_2 reduction. This was due to the defect levels that reduced the band gap and accelerated charge transfer.

Ghahramanifard et al. conducted a study on photoelectrocatalysis, using Cu-doped ZnO nanorods (NRs).[123] They electrodeposited p-type Cu-doped ZnO NRs on FTO glass, where Cu^{2+} substituted Zn^{2+} in the ZnO NRs hexagonal wurtzite structure. The XRD spectra of Cu-ZnO nanorods reveal the absence of Cu oxide or any contaminants. This suggests that the introduced Cu has likely replaced Zn^{2+} ions, without altering the hexagonal wurtzite structure of the ZnO nanorods. However, as the dopant (Cu^{2+}) concentration increased the peak intensity of the (002)

plane decreased, indicating that the incorporation impacts the crystallinity of the films since the crystal radius of Cu^{2+} (71 picometers) is lesser than that of Zn^{2+} (74 picometers). The UV-Vis analysis showed a clear improvement in the absorption of visible light in ZnO after Cu-doping, as a result of the decreased optical bandgap. In addition, Cu-doping leads to the formation of an acceptor level below the conduction band of ZnO. In the Mott-Schottky analysis, it is observed that the introduction of Cu ions (1.7 and 3.6%) to ZnO resulted in the role of substitutional Cu ions as acceptors, leading to a conversion of conductivity from n-type to p-type. Additionally, with the increase in Cu concentration, a reduction in the bandgap of ZnO was observed. Furthermore, the conduction band position of p-type Cu-doped ZnO became more negative, surpassing CO_2 reduction potential. This created a driving force for the reduction of CO_2. ZnO nanorods with 3.6% Cu-doping showed improved visible-light-driven CO_2 reduction, resulting in high current density at a low negative overpotential.

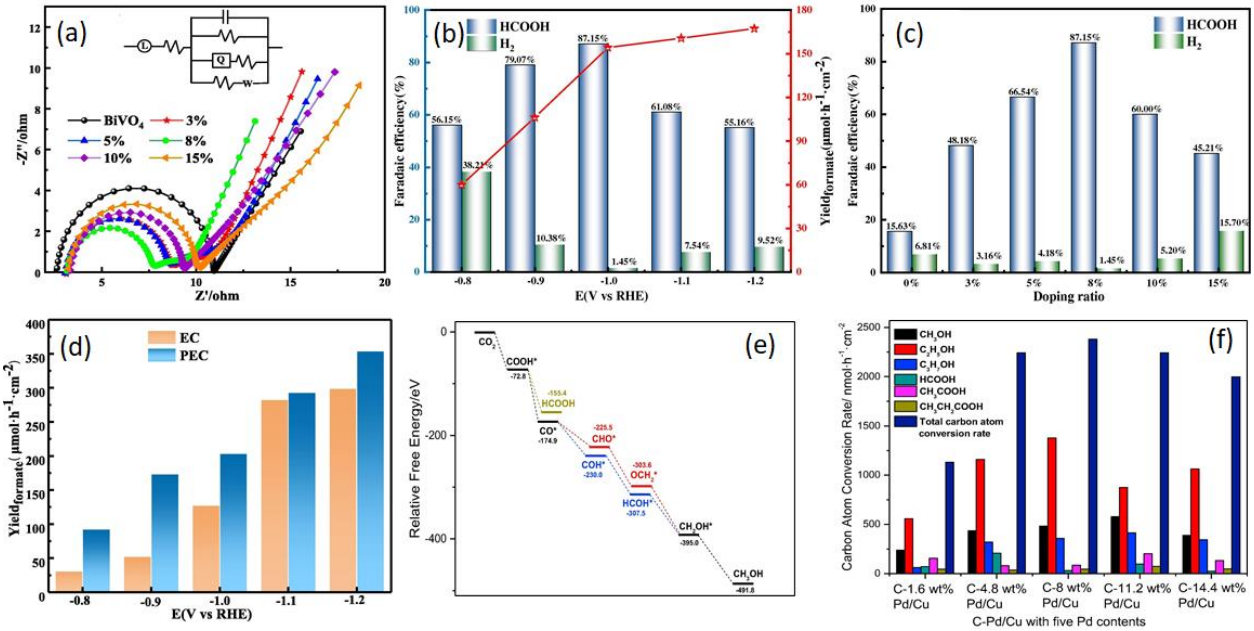

Figure 9: (a) EIS plots of $BiVO_4$ and Cu-$BiVO_4$ with different concentrations of Cu-doping (inset: the equivalent circuit impedance model), (b) Faradaic efficiency and formate yield of 8% Cu-

doped $BiVO_4$ EC CO_2 reduction, and (c) Formate yield in EC and PEC system using 8% Cu-doped $BiVO_4$, and (d) Stability test of 8% Cu-doped $BiVO_4$ at −1.0 V (vs. RHE). Taken with permission from[41], Copyright 2023, Elsevier. (e) CO_2 reduction free energy pathways to CH_3OH and HCOOH, and (f) CO_2 reduction over C-Pd/Cu catalysts with different Pd concentrations. Taken with permission from[124], Copyright 2019, Elsevier.

Cheng et al. reported the reaction of CO_2 reduction using the C-Pd/Cu catalyst.[124] In this investigation, the carbonization of Cu(BTC) doped with Pd NPs (designated as Pd@Cu(BTC)) was carried out to produce an octahedral C-Pd/Cu catalyst, aiming at selectively converting CO_2 into alcohols. The presence of Pd-doping in Cu was verified through XPS analysis. Raman analysis indicates that the C-Pd/Cu, characterized by defects, offers a higher number of active sites for intermediate adsorption and promotes electron transfer. It is well known that a theoretical understanding of density functional theory (DFT) calculation can offer a reliable approach to predicting the selectivity of CO_2 reduction. Cheng et al. also provided a set of DFT calculations on the Pd/Cu slab model surface. The study involved a comparison of the energy profiles of pathways leading to HCOOH and CH_3OH. The findings suggest that C-Pd/Cu exhibited a greater preference for methanol formation (CH_3OH) over formic acid formation (HCOOH). The relative free energy for CH_3OH formation was lower (19.5 eV) than for HCOOH formation, as shown in **Figure 9e**. Hence, the formation of CH_3OH follows $CO_2 \rightarrow COOH^* \rightarrow CO^* + H_2O \rightarrow COH^* \rightarrow HCOH^* \rightarrow CH_2OH^* \rightarrow CH_3OH$ pathway. Later on, catalytic tests were conducted for a CO_2 PE cell with a C-Pd/Cu catalyst as cathode and Pt-TiO_2 nanotubes (Pt-TNTs) as anode. The result showed that the optimized catalyst (C-8 wt.% Pd/Cu) showed a CO_2 reduction rate of 2380 nmol h^{-1} cm^{-2} (total carbon atom conversion), as shown in **Figure 9f**, and the alcohol selectivity reached

93.2%. The overall alcohol yield including CH_3OH, CH_3CH_2OH, and $CH_3CH_2CH_2OH$, reached 2217.8 nmol h^{-1} cm^{-2}.

Gu et al. synthesized Mg-doped $CuFeO_2$ using a solid-state method for PEC CO_2 reduction, which resulted in photocurrents of 1 mA cm^{-2} in CO_2-saturated 0.1 M $NaHCO_3$ (pH 6.8).[101] In bulk electrolysis experiments, formate was observed as the main reduction product under blue LED light illumination; however, no quantitative yield was shown. The faradaic efficiency for formate formation was only 10% at −0.9 V vs. SCE on Mg-doped $CuFeO_2$. Such a low faradaic efficiency was due to the competitiveness of H_2 evolution. The measurement of incident photon-to-current efficiencies (IPCE) was conducted on electrodes composed of Mg-doped $CuFeO_2$ at −0.4 V vs. SCE in a 0.1 M $NaHCO_3$ solution, with careful consideration given to minimizing the impact of dark current. An IPCE efficiency of 14% was recorded at the short wavelength (i.e., 340 nm), but this efficiency declined notably to 2% at longer wavelengths (780 nm). To observe the impact of Mg-doping on $CuFeO_2$ catalysis, an XRD analysis was conducted on the electrode before and after electrolysis. The XRD findings following 8 hours of electrolysis revealed the absence of noticeable Cu^0 on the surface, suggesting a sluggish Cu^0 production. Meanwhile, formate is detected before the 8 h reaction, signifying that Cu^0 on the electrode surface does not expedite formate generation, confirming that Mg-doped $CuFeO_2$ contributes to CO_2 conversion. In addition to the studies mentioned earlier, Sn has been successfully used as a dopant along with WO_3 to convert CO_2 into formic acid. WO_3 has a band gap of about 2.6 eV for CO_2 reduction reaction, and its valence band edge has sufficient potential to drive H_2O oxidation. However, WO_3's efficiency in CO_2 reduction is low due to charge recombination and poor OER kinetics. Therefore, doping the Sn, as an electron donor, could increase the carrier density of WO_3, enhancing the electrical conductivity. To this end, Sn-doped WO_3 films were studied for PEC CO_2 reduction into formic

acid.[125] Sn-doping to WO_3 resulted in the formation of 485 nmol cm^{-2} of HCOOH in 3 hours, which was more than twice as much as WO_3. The 5% Sn-WO_3 photoanode among various Sn-doped WO_3 films has the highest relative PEC performance; however, the activity was reduced with the increased concentration of Sn, which may be attributed to excess Sn, which may lead to charge recombination.

The buried junction, e.g., the p-n junction, architectures have also been widely studied to enhance the catalytic activities via increased band-bending within the bulk catalyst or PEC electrode surface. For example, constructing a p-n heterojunction may create an internal electric field, which provides electrostatic force to enhance charge transfer. Zhang et al. in 2020 reported such a p-n junction of Nb-doped TiO_2 nanotube arrays (TNNTs) with $CuFeO_2$.[126] TNNTs were produced through anodic oxidation of a TiNb alloy in a 0.5% HF solution. To assess the heat stability of the nanotubes, their morphology was examined following calcination at 650 °C. The findings suggest that the nanotube array structure remains intact after calcination, underscoring the significant enhancement in heat stability attributed to the presence of Nb in TNNTs. $CuFeO_2$ worked as a coating layer to a p-n junction leading to enhancement in the visible light absorption and photogenerated charge carriers. Interestingly, the change in the photocurrent response was observed with the coated amount of $CuFeO_2$ on TNNTs. Initially, the samples exhibit good photoresponse behavior, with photocurrents of 20 μA cm^{-2}. Photocurrents rose with the coating amount and reached 80 μA cm^{-2} at 1.8 g m^{-2} $CuFeO_2$. However, after coating 3.0 g m^{-2} of $CuFeO_2$, the photocurrent was dropped. As $CuFeO_2$ is less conductive, thicker coatings lead to a decrease in photocathode conductivity. CO_2 reduction for the $CuFeO_2$/TNNTs photocathode was performed, and ethanol (3.3 mol/5h) was produced as the major product after 5 hours of reaction. The selectivity changed to formaldehyde at a lower potential of −0.2 V as the CO_2 reduction to

formaldehyde is a two-electron transfer process. When the applied potential was lower (−0.4 V), ethanol production increased while formaldehyde production decreased. The HER begins when the applied potential is too low (−0.6 V). Furthermore, current efficiency reached 75% at −0.4V. This study emphasizes the higher hydrocarbon formation as a result of CO_2 reduction.

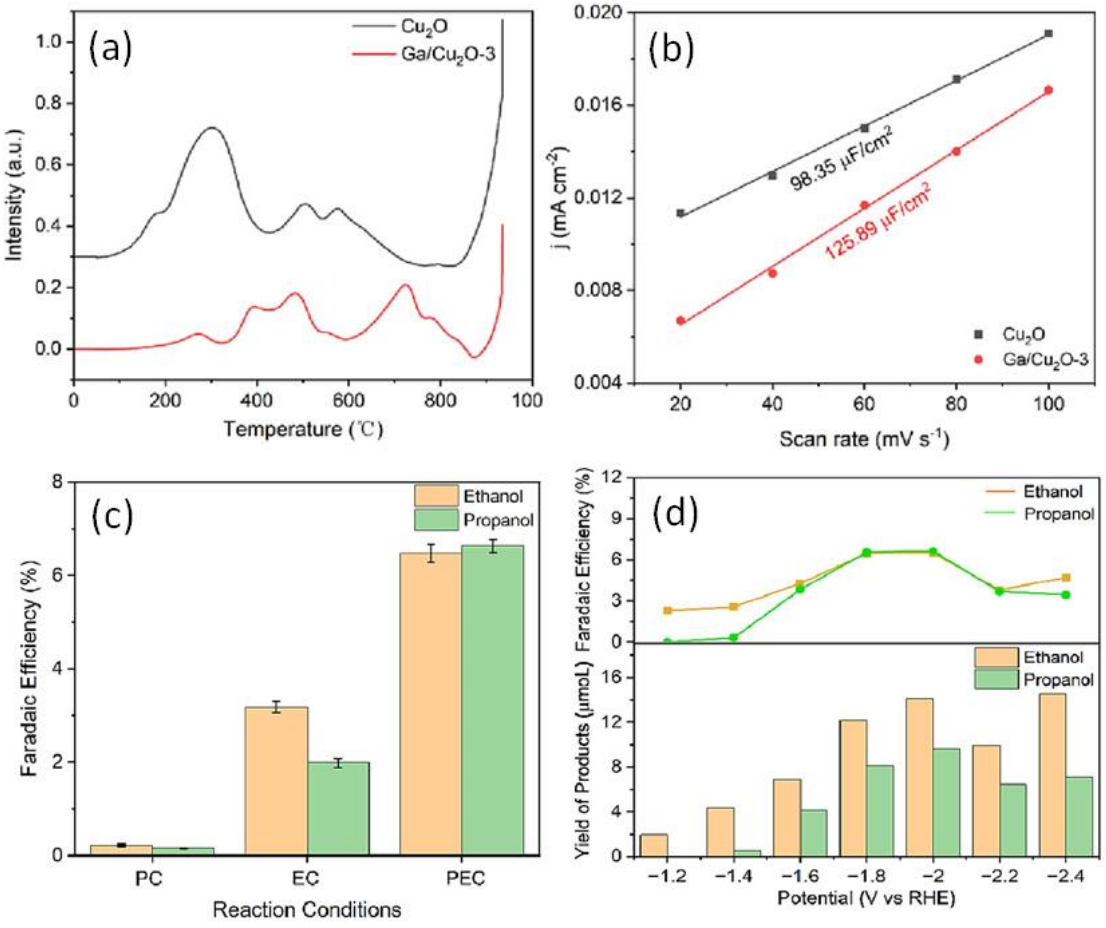

Figure 10: (a) CO_2-TPD and (b) double-layer capacitance of Cu_2O and Ga/Cu_2O-3, (c) faradaic efficiencies of ethanol and propanol over Ga/Cu_2O, and (d) product yield and faradaic efficiency (%) of the ethanol and propanol with Ga/Cu_2O-3 at −1.2 to −2.4 V vs. RHE. Taken with permission from[105], Copyright 2019, Elsevier.

Yang et al. reported PEC CO_2 reduction using Gallium (Ga)-doped Cu_2O aimed at enhancing the generation of C_{2+} products.[105] The introduction of Ga through partial substitution in the Cu_2O

lattice resulted in an increased number of O-vacancies, thereby influencing the electronic structure of the catalyst's surface. This modulation facilitated the regulation of CO_2 adsorption and activation. CO_2-TPD (temperature programmed desorption) results indicated that Ga-doped Cu_2O exhibited three desorption peaks and Cu_2O has two main desorption peaks. This result suggests that Ga-doping created a higher density of CO_2 adsorption sites than Cu_2O, as shown in **Figure 10a**. Notably, the double-layer capacitance value for Ga-doped Cu_2O (125.89 μF cm^{-2}) surpassed that of undoped Cu_2O (98.35 μF cm^{-2}), indicating that Ga-doping significantly expanded the electrochemical active surface area **(Figure 10b**). Furthermore, Ga-doping significantly affected improved charge separation and suppressed charge recombination. Consequently, the faradaic efficiencies for ethanol and propanol in the PEC system were 6.5% and 6.64%, respectively at −1.8 V vs. RHE, surpassing the efficiencies in PC and EC systems (**Figure 10c**). The superiority of PEC CO_2 reduction over PC and EC systems stemmed from the generation of additional electrons during light irradiation over Ga-doped Cu_2O. The faradaic efficiencies for ethanol and propanol formation were 1.53 and 1.49 times higher in Ga-doped Cu_2O than pristine Cu_2O. Interestingly, at a lower potential of −1.2 V vs. RHE, only ethanol was produced, while higher hydrocarbon formation occurred as the potential increased from −1.2 V to −2.0 V vs. RHE, as depicted in **Figure 10d**. This study introduces a strategy for designing metal-doped catalysts to efficiently generate C_{2+} products in PEC CO_2 reduction.

Several studies have been conducted combining TiO_2 with graphene oxide combination for catalytic applications. TiO_2/graphene oxide significantly improves the absorption in the visible region, improves CO_2 adsorption, and enhances the charge separation ability for catalytic reactions[127]. Apart from such binary electrode materials, ternary composites have also been investigated for PEC CO_2 reduction. For example, Hasan and colleagues fabricated a

nanocomposite comprising Ga–RGO–TiO_2 through a straightforward sol-gel method on an ITO substrate using electrophoretic deposition.[128] A thin film catalyst was prepared and placed in a cubic quartz cell of a PEC reactor to reduce CO_2 under the illumination of solar light. Combining RGO with Ga-doped TiO_2 enhances light absorption and charge separation, improving CO_2 reduction. The findings indicated that the main outcomes of photoreduction were formic acid, accompanied by minor quantities of methanol. The Ga-RGO-TiO_2/ITO photoelectrode generated the highest photocurrent, reaching 4.6 mA at −0.57 V vs. SCE. In contrast, the TiO_2 or RGO-TiO_2 thin film photoelectrodes did not produce any significant photocurrent. The maximum amount of formic acid produced during a 120-minute reaction was 178 ppm. **Table 1** represents the summaries of the various materials discussed in the review article.

5. Summary and Outlook

So far, several catalytic systems have been explored for the efficient conversion of CO_2 into value-added chemicals. The utilization of combined solar light and electricity, i.e., photoelectrochemical (PEC) conversion, has garnered significant interest as a clean and sustainable approach for CO_2 recycling. Electrode materials like metal oxides, metal hydroxides, metal chalcogenides, hybrid nanocomposites, and 2D materials, have shown promising PEC CO_2 conversion to improve the catalytic conversion and achieve high product selectivity of PEC CO_2 reduction reactions. Various strategies such as heterojunction formation, p-n junction, elemental doping, and metal NPs deposition on semiconductors have been investigated to further improve the catalytic activity of reaction. In this regard, elemental doped electrode materials (featuring non-metals such as O, N, and S and metals such as Fe, Co, Ni, and Cu) for the conversion of CO_2 through photoelectrocatalysis have also been investigated to enhance the optoelectronic properties of the materials. Elemental doped catalysts feature vacancy formation, tune the electronic band,

extend the light absorption in the visible region, improve the charge separation, and ultimately enhance the PEC CO_2 reduction. Specifically, catalysts containing elemental copper have surfaced as favorable choices for catalysis due to their ability to enhance optoelectronic properties and environmentally friendly characteristics. Additionally, electrode materials based on copper have demonstrated elevated activity, sustained stability, and increased selectivity towards higher hydrocarbons. Hence, it is logical to conclude that electrode materials containing copper can be fine-tuned to attain improved catalytic activity with higher carbon product formation.

Metal-doped photoelectrode materials offer key advantages for the PEC CO_2 reduction reactions. Alongside these benefits, there are notable downsides to consider. In comparison to electrochemical CO_2 conversion, there has been a lack of studies on PEC CO_2 reduction using these materials. The existing challenge lies in the insufficient efficiency of catalytic conversion and the selectivity of CO_2 reduction reactions, hindering their practical and widespread implementation. Current research mainly covers single-element doped catalysts. We should explore novel materials like single-atom catalysts (SACs) or dual-element doping to improve efficiency and control selection. For instance, Pengsong Li et al. conducted a study where they synthesized a combination of Ag and S doped onto Cu_2O/Cu host material[129]. The study revealed that S doping altered the electronic structure and morphology of the catalysts, which favored methanol formation. On the other hand, Ag suppressed the HER. Hence, dual doping significantly improved the activity and selectivity of electrochemical CO_2 reduction to methanol. Research in the field of PEC CO_2 conversion predominantly emphasizes achieving high catalytic activity. However, there exists a notable gap in our understanding of the factors responsible for diminished catalytic activity and catalyst deactivation. To tackle these challenges, employing in-situ analysis and theoretical calculations becomes crucial. The issue of reduced active sites for CO_2 reduction

arises from the excessive introduction of elemental dopants, leading to surface passivation or unwanted side reactions. Thus, controlled doping under optimized reaction conditions poses a significant challenge. Although high temperatures are necessary for element doping, they can inadvertently result in dopant aggregation, serving as charge recombination centers. Long-term stability issues, particularly under extended exposure to light, confront doped photoelectrode materials. Therefore, ensuring the long-term stability and robustness of elemental-doped catalysts in aqueous systems is important for practical applications. The scale-up of elemental-doped photoelectrode material synthesis while maintaining performance and cost-effectiveness presents a substantial obstacle. Addressing all these challenges is essential for proceeding with the practical application of metal-doped photoelectrode materials in photoelectrocatalytic CO_2 reduction reactions. In addition to material design, further research should be directed towards optimization of operating conditions and reactor upscaling.

Overall, the photoelectrochemical conversion of CO_2 into fuels is an increasingly compelling scientific topic, holding significant promise for industrial-scale implementation. This technology presents a potential facet of the solution to the challenges posed by global warming and energy demands. It is imperative for researchers to actively engage in interdisciplinary collaborations to effectively address existing issues. Through ongoing studies, our collective efforts can contribute to the continual enhancement of knowledge, bringing us closer to the development of an efficient PEC system for renewable energy.

Table 1: Summary of elemental doped electrode materials for PEC CO_2 reduction, detailing catalysts, reaction condition, catalytic performance (product yield, faradaic efficiency (FE), and photocurrent density).

Catalysts	Reaction conditions	Product yield, FE%, Photocurrent density, Selectivity, and Photocurrent stability	Remark	Year of publication [Ref.]
Oxygen-incorporated C_3N_4 (CN)	Three electrode system, 0.5 mol L^{-1} Na_2SO_4, a bias of −0.9 V vs. RHE, 300 Xe lamp	HCOOH: 273.56 µmol cm^{-2} h^{-1}, Photocurrent density: 587 µA cm^{-2}	Product selectivity and long-term stability have not been discussed.	2022[112]
CZTS/CdS (Oxygen doped CdS)	H-type cell, CO_2-saturated 0.1 m $KHCO_3$, standard potential of Ag/AgCl: 0.1976 V, Light of 100 mW cm^{-2}	CO: ~4.0 µmol cm^{-2} h^{-1} at -0.8 V vs. RHE, CH_3OH+CH_3CH_2OH: ~5.5 µmol cm^{-2} h^{-1} at -0.4 V vs. RHE	Stability has not been discussed.	2021[114]
S-Cu_2O/CuO	Three electrode system, 0.25 M $NaHCO_3$, bias potential of 0.47 V vs. RHE, 1W LED lamp	CH_3OH: 32 µmol cm^{-2} h^{-1}, FE of CH_3OH: 39%, CH_3COCH_3: 22 µmol cm^{-2} h^{-1}, FE of CH_3COCH_3: 35.7%, Photocurrent stability: 8000 s	The CO_2 reduction reaction was carried out using a 1-watt LED lamp. FE% is low for higher hydrocarbons.	2017[104]
S, N-codoped Nanoporous Carbon	0.1M $KHCO_3$, bias potential of 0.67 V vs. RHE, 150 W Xe lamp	CO: 15.8 µmol h^{-1}, FE of CO: 27.0%, 5 h, Stability: 12 h at -0.84 V	Product selectivity has not been discussed (due to the scope of this paper) although ^{1}H NMR detected methanol, formic acid, and acetone.	2018[130]
N-doped carbon/N-doped ZnO@ZnTe nanorods (N:C/N:ZnTe)	CO_2-saturated 0.5 m $KHCO_3$, 1 sun illumination (100 mW cm^{-2}), DC potential of −0.11 V vs. RHE	CO: 40.99 µmol cm^{-2}, FE of CO: 71.65% at −0.11 V_{RHE} after 3 h, CO selectivity: 78.17%	A significant amount of H_2 evolution of 11.54 µmol cm^{-2} and FE of 20.01%	2018[40]
Au-B-C_3N_4 (Au-BCN)	0.5 M $NaHCO_3$, −0.4 V vs. Ag/AgCl, AM 1.5 G solar-simulated system	C_2H_5OH: ~150 nmol, $FE_{Au\text{-}BCN}$ of C_2H_5OH: 47%, FE_{BCN} of C_2H_5OH: 78%, CO: ~20 nmol, $FE_{Au\text{-}BCN}$ of CO: 0.9%, FE_{BCN} of CO: 0.7%	Low catalytic activity. Small amounts of CO and H_2 were observed in the gas phase.	2016[110]
Zn-Cu_2O (Au/N-TiO_2 photoanode)	H-type quartz reactor, 0.5 mol L^{-1} Na_2SO_4 and 0.1 mol L^{-1} $KHCO_3$, 200 mW cm^{-2} illumination	CH_3COOH: 1.1 µmol/6h (output potential 1.5 V), FE of CH_3COOH: 58.4% at .5 V vs. Ag/AgCl CH_3COOH selectvity: 91.5%	Au-loaded N-doped TiO_2 plate array was used as a photoanode while Zn-doped Cu_2O used a dark cathode. The long-term stability of the reaction has not been carried out.	2021[52]
(Bi, S)-SnO_2	0.5 M $NaHCO_3$, onset potential of −0.88 V vs. SHE	Current density: 9.33 mA cm^{-2} at −1.4 V vs. Ag/AgCl, FE of formate: 55.6%, Current stability:10 h at −1.0 V in CO_2 and N_2	The amount of formate formation and product selectivity has not been detected.	2019[109]
Co-MoS_2	A sealed two-cell reactor, 0.1 M $KHCO_3$, 500 W Xe lamp	CH_3OH: 35 mmol L^{-1} at −0.9 eV	The product selectivity has not been discussed.	2015[118]

			Stability (current density) was shown for 1200 s.	
Co-CdS QDs	H-type cell, 0.5 M $KHCO_3$, PLS-FX300 HU Xenon lamp	FE of HCOOH: 82.9%, photocathode stability: 180 min, Photocurrent density: −2.6 mA cm^{-2} at −0.75 vs. RHE	The quantitative analysis of the products is not mentioned.	2024 [119]
Cu-RGO–TiO_2	Cubic quartz photoelectrochemical cell, 0.1 M Na_2SO_4, CO_2 saturated 10% methyl diethanolamine (MDEA), -0.61 V vs. SCE, 150 W Xe arc lamp	HCOOH: 255 μmol h^{-1} cm^{-2}, CH_3OH: 189.06 μmol h^{-1} cm^{-2}, Photocurrent density: 1.31 mA cm^{-2} at −0.61 V vs. SCE	Longer reaction time forms CH_3OH. The photocurrent density fluctuated during the reaction. Initial photocurrent density (4.56 mA cm^{-2}) was significantly decreased (0.63 mA cm^{-2}) at the end of the reaction (6 h)	2015[121]
Cu-doped Bi_2Se_3	H-type cell, CO_2-saturated 0.5 M $NaHCO_3$, 300 W Xe lamp	$HCOO^-$: 139.97 μmol h^{-1} cm^{-2}, FE of $HCOO^-$: 65.31% at ~500 mV vs. RHE, Current density: −24.14 mA cm^{-2} at −1.3 V vs. RHE, Stability: 24 h (current density)	$HCOO^-$ was the only liquid product observed during the CO_2 reduction reaction. A significant amount of $HCOO^-$ was reported without light illumination (111.18 μmol h^{-1} cm^{-2})	2022[107]
Cu-doped $BiVO_4$	H-type electrolytic cell, CO_2 saturated 0.5 mol L^{-1} $NaHCO_3$, 300 W Xe lamp	HCOOH: 354.26 μmol $h^{-1}cm^{-2}$, FE of HCOOH: 87.15 % at −1.0 V vs. RHE, Current density: −20.68 mA cm^{-2} at −1.3 V vs. RHE, Stability: 24 h	$HCOO^-$ was the only liquid product observed during the CO_2 reduction reaction.	2023[41]
(Cu, N)-SnO_x	H-type cell, 0.5 mol/L $NaHCO_3$ solution saturated with CO_2, 300 W Xe lamp	HCOOH: 617.35 mg L^{-1}, Current density: 12 mA cm^{-2} at −1.6 V, Potential: 1.4 V vs. Ag/AgCl	FE (54.97%) was low compared to several SnO_2-based materials.	2020[108]
Cu-SnO_2/ZIF-8	H-type cell, 0.5M $NaHCO_3$, 300 W Xe lamp	FE of HCOOH: 68.96%, Overpotential: ~364 mV, Current density: 12.8 mA cm^{-2} at −1.4V vs. Ag/AgCl, Electrolysis stability: 10 h at −1.0 V vs. Ag/AgCl	The quantitative analysis of the products is not mentioned.	2021[122]
Cu/ZnO NRs	Single compartment sealed glass cell, 0.1 M tetrabutylammonium hexafluorophosphate (TBAHP), 100 W LED light	Photocurrent: 500 mA cm^{-2} at −0.5 V vs. NHE	The photoelectrocalytic property of the catalysts has been carried out, but quantitative measurement of the CO_2 reduction reaction has not been shown.	2018[123]
C-Pd NPs/Cu	H-shaped double chamber reactor, PLS-SXE300CUV Xe lamp, 0.5 M H_2SO_4 (anolyte), 0.5 M $NaHCO_3$ (catholyte)	Total carbon atom conversion: 2380 nmol h^{-1} cm^{-2}, CH_3OH + CH_3CH_2OH + $CH_3CH_2CH_2OH$: 2217.8 nmol h^{-1} cm^{-2} (Selectivity: 93.2%) Photocurrent density: 2.8 mA cm^{-2}	The stability of current density stability was decreased after 2 h from ~2.8 mA cm^{-2} to ~1.7 mA cm^{-2} and lasted for 12 h.	2019[124]
Mg- $CuFeO_2$	Pyrex test tube, 0.1 M $NaHCO_3$, 75 W Xe Arc lamp	FE of HCOOH: 10% at −0.9 V vs. SCE, IPCE: 14% at 340 nm at −0.4 V vs. SCE	Quantitative CO_2 conversion efficiency was not determined.	2013[101]

			H_2 production was predicted as a side reaction at −0.9 V vs. SCE.	
Sn-doped WO_3	H-type cell, 0.2 M Na_2SO_4 electrolyte in anodic chamber and CO_2-saturated 0.5 M $KHCO_3$, 150 W Xe lamp (400-nm cutoff filter)	HCOOH: 485 nmol cm^{-2} (3 h), Photocurrent density: 1.11 mA cm^{-2} at 1.2 V vs. Ag/AgCl, IPCE: 45.1% at 350 nm	The stability of the catalyst has not been carried out. A small amount of water splitting was observed.	2017[125]
Nb-doped TiO_2 ($CuFeO_2$/TNNTs)	80 ml gas-tight glass container, 0.1 mol/L $NaHCO_3$, 250 W Xe lamp	HCHO: 2.0 µmol at −0.2 V, CH_3CH_2OH: 3.3 µmol at −0.4 V, FE: 75% at −0.4 V, Photocurrent: 80 µA cm^{-2}	When the potential exceeds -0.6 V, the current increases suddenly due to H_2 evolution.	2020[126]
Ga/Cu_2O	H type cell, Nafion 117 proton exchange membrane, CO_2 saturated 0.1 M $KHCO_3$ solution, 300 W Xe lamp ($400 \leq \lambda \leq 800$ nm)	C_2H_5OH: 14.13 µmoL, FE of C_2H_5OH: 6.50%, C_3H_7OH: 6.50 µmoL, FE of C_3H_7OH: 6.64%, Photocurrent: 13.23 mA cm^{-2}	Along with ethanol and propanol as main products, the PEC CO_2 reduction also showed activity towards CO, C_2H_4, CH_4, C_2H_6, and H_2.	2023[105]
Ga-RGO–TiO_2	A cubic quartz cell, 5% triethanolamine (TEA) CO_2 saturated solution, light intensity: 10 mW cm^{-2}	HCOOH: 178 ppm (2 h), Photocurrent: 4.6 mA at −0.57 V vs. SCE	The photocurrent was significantly dropped from 4.6 mA to 1.65 mA during the first 30 min.	2015[128]

Acknowledgments

This work was supported by the National Research Foundation of Korea (NRF; 2021M3I3A1085039). DB, JK, and CBH acknowledge the British Council for the financial support (Reconnect Programme). Additionally, DB and JK also thank the Engineering and Physical Sciences Research Council of the UK (EPSRC; EP/X015920/1) and Royal Society (RGS\R2\222374) for the financial supports.

Received: ((will be filled in by the editorial staff))
Revised: ((will be filled in by the editorial staff))
Published online: ((will be filled in by the editorial staff))

References

[1] J. Ran, M. Jaroniec, S. Qiao, *Adv. Mater.* **2018**, *30*, 1704649.

[2] C. B. Hiragond, S. Biswas, N. S. Powar, J. Lee, E. Gong, H. Kim, H. S. Kim, J. Jung, C. Cho, B. M. Wong, *Carbon Energy* **2023**, e386.

[3] C. B. Hiragond, N. S. Powar, J. Lee, S. In, *Small* **2022**, 2201428.

[4] N. S. Powar, M. Jang, M. G. Kim, C. B. Hiragond, J. Lee, E. Gong, H. Kim, D. Kim, J.-W. Jung, C.-H. Cho, *Chem. Eng. J.* **2023**, 147966.

[5] Y. H. Park, D. Kim, C. B. Hiragond, J. Lee, J.-W. Jung, C.-H. Cho, I. In, S.-I. In, *J. CO2 Util.* **2023**, *67*, 102324.

[6] W. Tu, Y. Zhou, Z. Zou, *Adv. Mater.* **2014**, *26*, 4607.

[7] K. Li, B. Peng, T. Peng, *ACS Catal.* **2016**, *6*, 7485.

[8] W. Zhang, Y. Hu, L. Ma, G. Zhu, Y. Wang, X. Xue, R. Chen, S. Yang, Z. Jin, *Adv. Sci.* **2018**, *5*, 1700275.

[9] S. Das, J. Pérez-Ramírez, J. Gong, N. Dewangan, K. Hidajat, B. C. Gates, S. Kawi, *Chem. Soc. Rev.* **2020**, *49*, 2937.

[10] S. De, A. Dokania, A. Ramirez, J. Gascon, *ACS Catal.* **2020**, *10*, 14147.

[11] S. Guo, T. Asset, P. Atanassov, *ACS Catal.* **2021**, *11*, 5172.

[12] F. O. Ochedi, D. Liu, J. Yu, A. Hussain, Y. Liu, *Environ. Chem. Lett.* **2021**, *19*, 941.

[13] P. Wang, S. Wang, H. Wang, Z. Wu, L. Wang, *Part. Part. Syst. Charact.* **2018**, *35*, 1700371.

[14] Y. Wang, D. He, H. Chen, D. Wang, *J. Photochem. Photobiol. C Photochem. Rev.* **2019**, *40*, 117.

[15] S. Xu, Q. Shen, J. Zheng, Z. Wang, X. Pan, N. Yang, G. Zhao, *Adv. Sci.* **2022**, *9*, 2203941.

[16] J. F. de Brito, G. G. Bessegato, J. A. L. Perini, L. D. de Moura Torquato, M. V. B. Zanoni, *J. CO2 Util.* **2022**, *55*, 101810.

[17] Y. Yan, J. Gu, E. L. Zeitler, A. B. Bocarsly, In *Carbon Dioxide Utilisation*; Elsevier, 2015; pp. 211–233.

[18] P. Chen, Y. Zhang, Y. Zhou, F. Dong, *Nano Mater. Sci.* **2021**, *3*, 344.

[19] H. Kim, J. W. Seo, W. Chung, G. M. Narejo, S. W. Koo, J. S. Han, J. Yang, J. Kim, S. In, *ChemSusChem* **2023**, e202202017.

[20] L. Liu, Y. Zhang, H. Huang, *Sol. RRL* **2021**, *5*, 2000430.

[21] N. Dhabarde, J. Selvaraj, A. Yuda, A. Kumar, V. R. Subramanian, *Int. J. Hydrogen Energy* **2022**, *47*, 30908.

[22] B. Han, J. Wang, C. Yan, Y. Dong, Y. Xu, R. Nie, H. Jing, *Electrochim. Acta* **2018**, *285*, 23.

[23] J.-Y. Liu, X.-Q. Gong, R. Li, H. Shi, S. B. Cronin, A. N. Alexandrova, *ACS Catal.* **2020**, *10*, 4048.

[24] Z. Otgonbayar, W.-C. Oh, *J. Inorg. Organomet. Polym. Mater.* **2022**, *32*, 2910.

[25] J. Y. Zheng, A. U. Pawar, Y. S. Kang, *Catalysts* **2022**, *12*, 1399.

[26] K. M. Rezaul Karim, M. Tarek, H. R. Ong, H. Abdullah, A. Yousuf, C. K. Cheng, M. M. R. Khan, *Ind. Eng. Chem. Res.* **2018**, *58*, 563.

[27] J. Liu, C. Guo, X. Hu, G. Zhao, *Green Chem.* **2019**, *21*, 339.

[28] J. W. Maina, C. Pozo-Gonzalo, J. A. Schütz, J. Wang, L. F. Dumée, *Carbon N. Y.* **2019**, *148*, 80.

[29] X. Wu, R. Xu, X. Li, R. Zeng, B. Luo, *J. Phys. Chem. C* **2022**, *126*, 15744.

[30] Z. Otgonbayar, C.-M. Yoon, W.-C. Oh, *Chem. Eng. J.* **2023**, *464*, 142716.

[31] M. Kan, Q. Wang, S. Hao, A. Guan, Y. Chen, Q. Zhang, Q. Han, G. Zheng, *J. Phys. Chem. C* **2022**, *126*, 1689.

[32] J. Wang, Y. Wei, B. Yang, B. Wang, J. Chen, H. Jing, *J. Catal.* **2019**, *377*, 209.

[33] K. Xu, A. Chatzitakis, P. H. Backe, Q. Ruan, J. Tang, F. Rise, M. Bjørås, T. Norby, *Appl.*

Catal. B Environ. **2021**, *296*, 120349.

[34] S. Chu, P. Ou, P. Ghamari, S. Vanka, B. Zhou, I. Shih, J. Song, Z. Mi, *J. Am. Chem. Soc.* **2018**, *140*, 7869.

[35] L.-X. Liu, J. Fu, L.-P. Jiang, J.-R. Zhang, W. Zhu, Y. Lin, *ACS Appl. Mater. Interfaces* **2019**, *11*, 26024.

[36] A. Zhang, R. He, H. Li, Y. Chen, T. Kong, K. Li, H. Ju, J. Zhu, W. Zhu, J. Zeng, *Angew. Chemie Int. Ed.* **2018**, *57*, 10954.

[37] S. Chen, T. Liu, S. O. Olanrele, Z. Lian, C. Si, Z. Chen, B. Li, *J. Energy Chem.* **2021**, *54*, 143.

[38] A. Zhang, Y. Liang, H. Zhang, Z. Geng, J. Zeng, *Chem. Soc. Rev.* **2021**, *50*, 9817.

[39] J. Ran, T. Y. Ma, G. Gao, X.-W. Du, S. Z. Qiao, *Energy Environ. Sci.* **2015**, *8*, 3708.

[40] Y. J. Jang, M. D. Bhatt, J. Lee, S. H. Choi, B. J. Lee, J. S. Lee, *Adv. Energy Mater.* **2018**, *8*, 1702636.

[41] F. Gao, H. Yang, C. Nan, W. Zhou, N. Gao, Y. Jia, Y. Zhang, R. Chen, *J. Electroanal. Chem.* **2023**, *930*, 117146.

[42] E. Gong, S. Ali, C. B. Hiragond, H. S. Kim, N. S. Powar, D. Kim, H. Kim, S.-I. In, *Energy Environ. Sci.* **2022**.

[43] S. Ali, M. C. Flores, A. Razzaq, S. Sorcar, C. B. Hiragond, H. R. Kim, Y. H. Park, Y. Hwang, H. S. Kim, H. Kim, *Catalysts* **2019**, *9*, 727.

[44] C. Hiragond, S. Ali, S. Sorcar, S.-I. In, *Catalysts* **2019**, *9*, 370.

[45] N. S. Powar, C. B. Hiragond, D. Bae, S.-I. In, *J. CO2 Util.* **2022**, *55*, 101814.

[46] C. B. Hiragond, N. S. Powar, S.-I. In, *Nanomaterials* **2020**, *10*, 2569.

[47] V. Kumaravel, J. Bartlett, S. C. Pillai, *ACS Energy Lett.* **2020**, *5*, 486.

[48] B. Tang, F.-X. Xiao, *ACS Catal.* **2022**, *12*, 9023.

[49] K. Wang, Y. Ma, Y. Liu, W. Qiu, Q. Wang, X. Yang, M. Liu, X. Qiu, W. Li, J. Li, *Green*

Chem. **2021**, *23*, 3207.

[50] L. Xiao, C. Yuan, P. Chen, Y. Liu, J. Sheng, S. Zhang, F. Dong, Y. Sun, *ACS Sustain. Chem. Eng.* **2022**, *10*, 11902.

[51] A. U. Pawar, C. W. Kim, M.-T. Nguyen-Le, Y. S. Kang, *ACS Sustain. Chem. Eng.* **2019**, *7*, 7431.

[52] X. Wang, C. Gao, J. Low, K. Mao, D. Duan, S. Chen, R. Ye, Y. Qiu, J. Ma, X. Zheng, *Sci. Bull.* **2021**, *66*, 1296.

[53] A. S. Kumar, M. Pupo, K. V Petrov, M. Ramdin, J. R. van Ommen, W. de Jong, R. Kortlever, *J. Phys. Chem. C* **2023**, *127*, 12857.

[54] Y. Gao, X. Wang, H. Guo, L. Liu, H. Wang, W. Cui, *Mol. Catal.* **2023**, *543*, 113161.

[55] H.-K. Lim, Y. Kwon, H. S. Kim, J. Jeon, Y.-H. Kim, J.-A. Lim, B.-S. Kim, J. Choi, H. Kim, *ACS Catal.* **2018**, *8*, 2420.

[56] B. A. Rosen, A. Salehi-Khojin, M. R. Thorson, W. Zhu, D. T. Whipple, P. J. A. Kenis, R. I. Masel, *Science (80-.).* **2011**, *334*, 643.

[57] Y. Wang, M. Hatakeyama, K. Ogata, M. Wakabayashi, F. Jin, S. Nakamura, *Phys. Chem. Chem. Phys.* **2015**, *17*, 23521.

[58] S. A. S. Mohammed, W. Z. N. Yahya, M. A. Bustam, M. G. Kibria, *Separations* **2023**, *10*, 192.

[59] H. Zhao, G. A. Baker, *Green Chem. Lett. Rev.* **2023**, *16*, 2149280.

[60] L. K. Putri, B. Ng, W. Ong, S. Chai, A. R. Mohamed, *Adv. Energy Mater.* **2022**, *12*, 2201093.

[61] H. Kim, A. Choe, S. B. Ha, G. M. Narejo, S. W. Koo, J. S. Han, W. Chung, J. Kim, J. Yang, S. In, *ChemSusChem* **2023**, *16*, e202201925.

[62] J. Böckris, A. Reddy, M. Gamboa-Aldeco, *Mod. Electrochem. 2A Fundam. Electrodics* **2000**.

[63] P. Wu, J. Pan, X. Li, X. Hou, J. Xu, H. Chen, *Chem. Eur. J.* **2015**, *21*, 5129.

[64] P. Ding, T. Jiang, N. Han, Y. Li, *Mater. Today Nano* **2020**, *10*, 100077.

[65] J. S. DuChene, G. Tagliabue, A. J. Welch, W.-H. Cheng, H. A. Atwater, *Nano Lett.* **2018**, *18*, 2545.

[66] Y. Hu, F. Chen, P. Ding, H. Yang, J. Chen, C. Zha, Y. Li, *J. Mater. Chem. A* **2018**, *6*, 21906.

[67] Q. Shen, Z. Chen, X. Huang, M. Liu, G. Zhao, *Environ. Sci. Technol.* **2015**, *49*, 5828.

[68] S. K. Choi, U. Kang, S. Lee, D. J. Ham, S. M. Ji, H. Park, *Adv. Energy Mater.* **2014**, *4*, 1301614.

[69] P. Hu, S. Wang, Y. Zhuo, *Sep. Purif. Technol.* **2021**, *276*, 119323.

[70] J. H. Cho, C. Lee, S. H. Hong, H. Y. Jang, S. Back, M. Seo, M. Lee, H. Min, Y. Choi, Y. J. Jang, *Adv. Mater.* **2023**, *35*, 2208224.

[71] C. Tang, C. Chen, W. Xu, L. Xu, *J. Mater. Chem. A* **2019**, *7*, 6911.

[72] S. Shyamal, S. K. Dutta, N. Pradhan, *J. Phys. Chem. Lett.* **2019**.

[73] H. Ait Ahsaine, M. Zbair, A. BaQais, M. Arab, *Catalysts* **2022**, *12*, 450.

[74] D. Wang, J. Mao, C. Zhang, J. Zhang, J. Li, Y. Zhang, Y. Zhu, *eScience* **2023**, 100119.

[75] C. Kim, J. C. Bui, X. Luo, J. K. Cooper, A. Kusoglu, A. Z. Weber, A. T. Bell, *Nat. Energy* **2021**, *6*, 1026.

[76] G. P. S. Lau, M. Schreier, D. Vasilyev, R. Scopelliti, M. Gratzel, P. J. Dyson, *J. Am. Chem. Soc.* **2016**, *138*, 7820.

[77] S. Neyrizi, J. Kiewiet, M. A. Hempenius, G. Mul, *ACS Energy Lett.* **2022**, *7*, 3439.

[78] L. Ge, H. Rabiee, M. Li, S. Subramanian, Y. Zheng, J. H. Lee, T. Burdyny, H. Wang, *Chem* **2022**, *8*, 663.

[79] A. N. Frumkin, *Trans. Faraday Soc.* **1959**, *55*, 156.

[80] M. R. Singh, Y. Kwon, Y. Lum, J. W. Ager III, A. T. Bell, *J. Am. Chem. Soc.* **2016**, *138*, 13006.

[81] D. Bae, B. Seger, P. C. K. Vesborg, O. Hansen, I. Chorkendorff, *Chem. Soc. Rev.* **2017**, *46*, 1933.

[82] Q. Wang, J. Liu, Q. Li, J. Yang, *ChemSusChem* **2023**, e202202186.

[83] L. Yao, N. Guijarro, F. Boudoire, Y. Liu, A. Rahmanudin, R. A. Wells, A. Sekar, H.-H. Cho, J.-H. Yum, F. Le Formal, *J. Am. Chem. Soc.* **2020**, *142*, 7795.

[84] Y. Mao, H. Zhang, W. Jiang, R. Zhao, Y. Liu, Z. Wang, P. Wang, Z. Zheng, K. Song, W. Wei, *Nano Energy* **2022**, *102*, 107639.

[85] D. S. Kim, Y. B. Kim, J. H. Choi, H. W. Suh, H. H. Lee, K. W. Lee, S. H. Jung, J. J. Kim, N. G. Deshpande, H. K. Cho, *Adv. Energy Mater.* **2021**, *11*, 2170152.

[86] B. Shan, S. Vanka, T.-T. Li, L. Troian-Gautier, M. K. Brennaman, Z. Mi, T. J. Meyer, *Nat. Energy* **2019**, *4*, 290.

[87] J. J. Leung, J. Warnan, K. H. Ly, N. Heidary, D. H. Nam, M. F. Kuehnel, E. Reisner, *Nat. Catal.* **2019**, *2*, 354.

[88] M. Sassenburg, M. Kelly, S. Subramanian, W. A. Smith, T. Burdyny, *ACS Energy Lett.* **2022**, *8*, 321.

[89] B. Endrődi, A. Samu, E. Kecsenovity, T. Halmágyi, D. Sebők, C. Janáky, *Nat. energy* **2021**, *6*, 439.

[90] Z. Yin, H. Peng, X. Wei, H. Zhou, J. Gong, M. Huai, L. Xiao, G. Wang, J. Lu, L. Zhuang, *Energy Environ. Sci.* **2019**, *12*, 2455.

[91] J. Y. Zhao, Y. Liu, W. Li, C. F. Wen, H. Q. Fu, H. Y. Yuan, P. F. Liu, H. G. Yang, *Chem Catal.* **2023**, *3*.

[92] C. F. Wen, F. Mao, Y. Liu, X. Y. Zhang, H. Q. Fu, L. R. Zheng, P. F. Liu, H. G. Yang, *ACS Catal.* **2019**, *10*, 1086.

[93] J. Huo, Y. Zhang, W. Kang, Y. Shen, X. Li, Z. Yan, Y. Pan, W. Sun, *Nanoscale Adv.* **2023**.

[94] M. Crișan, M. Răileanu, N. Drăgan, D. Crișan, A. Ianculescu, I. Niţoi, P. Oancea, S. Şomăcescu, N. Stănică, B. Vasile, *Appl. Catal. A Gen.* **2015**, *504*, 130.

[95] J. A. Abarca, G. Díaz-Sainz, I. Merino-Garcia, A. Irabien, J. Albo, *J. Energy Chem.* **2023**.

[96] W. Zhang, Q. Zhou, N. Li, M. Li, *Appl. Catal. A Gen.* **2023**, *650*, 118977.

[97] I. Benammar, R. Salhi, J.-L. Deschanvres, R. Maalej, *J. Solid State Chem.* **2023**, *320*, 123856.

[98] G. Divya, G. Jaishree, T. Sivarao, K. V. D. Lakshmi, *RSC Adv.* **2023**, *13*, 8692.

[99] M. Miao, H. Duan, J. Luo, X. Wang, *Mater. Adv.* **2022**.

[100] C. An, F. Liu, J. Yuan, *Compos. Interfaces* **2021**, *28*, 1053.

[101] J. Gu, A. Wuttig, J. W. Krizan, Y. Hu, Z. M. Detweiler, R. J. Cava, A. B. Bocarsly, *J. Phys. Chem. C* **2013**, *117*, 12415.

[102] E. A. Fugate, S. Biswas, M. C. Clement, M. Kim, D. Kim, A. Asthagiri, L. R. Baker, *Nano Res.* **2019**, *12*, 2390.

[103] I. L. E. Gonzaga, C. C. Mercado, *Rev. Adv. Mater. Sci.* **2022**, *61*, 430.

[104] A. Navaee, A. Salimi, *J. Colloid Interface Sci.* **2017**, *505*, 241.

[105] X. Guo, C. Wang, Z. Yang, Y. Yang, *Chem. Eng. J.* **2023**, *471*, 144539.

[106] L. Yan, Z. Wu, C. Li, J. Wang, *J. Ind. Eng. Chem.* **2023**, *123*, 33.

[107] W. Zhou, H. Yang, N. Gao, D. Zhang, Z. Li, F. Gao, C. Nan, *J. Alloys Compd.* **2022**, *903*, 163707.

[108] H. Yang, Y. Li, D. Zhang, Z. Li, J. Wang, D. Yang, X. Hao, G. Guan, *Chem. Eng. Sci.* **2020**, *227*, 115947.

[109] Y. Li, H. Yang, X. Hu, H. Tian, M. Gao, D. Zhang, Z. Li, D. Yang, *ChemElectroChem* **2019**, *6*, 3782.

[110] N. Sagara, S. Kamimura, T. Tsubota, T. Ohno, *Appl. Catal. B Environ.* **2016**, *192*, 193.

[111] Y. Lu, H. Cao, S. Xu, W. Feng, G. Hou, Y. Tang, H. Zhang, G. Zheng, *J. Colloid Interface Sci.* **2021**, *599*, 497.

[112] H. Wang, Y. Zhao, Z. Yang, X. Bi, Z. Wang, M. Wu, *New Carbon Mater.* **2022**, *37*, 1135.

[113] H. Pang, X. Meng, H. Song, W. Zhou, G. Yang, H. Zhang, Y. Izumi, T. Takei, W. Jewasuwan, N. Fukata, *Appl. Catal. B Environ.* **2019**, *244*, 1013.

[114] S. Zhou, K. Sun, J. Huang, X. Lu, B. Xie, D. Zhang, J. N. Hart, C. Y. Toe, X. Hao, R. Amal, *Small* **2021**, *17*, 2100496.

[115] S. Gong, Y. Niu, X. Teng, X. Liu, M. Xu, C. Xu, T. J. Meyer, Z. Chen, *Appl. Catal. B Environ.* **2022**, *310*, 121333.

[116] F. W. Eagle, S. Harvey, R. Beck, X. Li, D. R. Gamelin, B. M. Cossairt, *ACS Nanosci. Au* **2023**.

[117] M. Z. Rahman, F. Raziq, H. Zhang, J. Gascon, *Angew. Chemie* **2023**, e202305385.

[118] H. Peng, J. Lu, C. Wu, Z. Yang, H. Chen, W. Song, P. Li, H. Yin, *Appl. Surf. Sci.* **2015**, *353*, 1003.

[119] S. Liu, Z. Guo, Y. Yang, P. Wu, Z. Li, K. Wang, H. Zhang, H. Li, S. Yang, *Environ. Chem. Lett.* **2024**, 1.

[120] Y. Zhou, F. Che, M. Liu, C. Zou, Z. Liang, P. De Luna, H. Yuan, J. Li, Z. Wang, H. Xie, *Nat. Chem.* **2018**, *10*, 974.

[121] M. R. Hasan, S. B. Abd Hamid, W. J. Basirun, S. H. M. Suhaimy, A. N. C. Mat, *RSC Adv.* **2015**, *5*, 77803.

[122] D. Zhang, H. Yang, Y. Li, Z. Li, N. Gao, W. Zhou, Z. Liang, *Int J Electrochem Sci* **2021**, *16*, 150951.

[123] F. Ghahramanifard, A. Rouhollahi, O. Fazlolahzadeh, *Superlattices Microstruct.* **2018**, *114*, 1.

[124] J. Cheng, X. Xuan, X. Yang, J. Zhou, K. Cen, *Chem. Eng. J.* **2019**, *358*, 860.

[125] Y. Yang, F. Zhan, H. Li, W. Liu, S. Yu, *J. Solid State Electrochem.* **2017**, *21*, 2231.

[126] L. Zhang, H. Cao, Y. Lu, H. Zhang, G. Hou, Y. Tang, G. Zheng, *J. Colloid Interface Sci.* **2020**, *568*, 198.

[127] C. B. Hiragond, J. Lee, H. Kim, J.-W. Jung, C.-H. Cho, S.-I. In, *Chem. Eng. J.* **2020**,

127978.

[128] M. R. Hasan, S. B. Abd Hamid, W. J. Basirun, Z. Z. Chowdhury, A. E. Kandjani, S. K. Bhargava, *New J. Chem.* **2015**, *39*, 369.

[129] P. Li, J. Bi, J. Liu, Q. Zhu, C. Chen, X. Sun, J. Zhang, B. Han, *Nat. Commun.* **2022**, *13*, 1965.

[130] W. Li, T. J. Bandosz, *ChemSusChem* **2018**, *11*, 2987.

Author Biographies:

Chaitanya B. Hiragond completed his Bachelor of Science in Chemistry from Shivaji University, India, in 2012, and Master of Science in Organic Chemistry at Bharati Vidyapeeth Deemed University, India, in 2014. He successfully obtained his Ph.D. in 2022 from the Daegu Gyeongbuk Institute of Science and Technology (DGIST) in the Republic of Korea. Currently, he serves as a postdoctoral researcher at the Department of Energy Science and Engineering, DGIST under the supervision of Prof. Su-Il In. His research is focused on heterogeneous catalysis for energy and environmental applications.

Jungmyung Kim is a PDRA in the Department of Engineering and Physical Sciences at Heriot-Watt University, UK. He received his doctorate in research related to redox flow batteries from the Department of Mechanical Engineering at Changwon National University, Republic of Korea, in 2021. Presently, he is dedicated to electrochemical analysis and the practical demonstration of secondary battery technologies.

Hwapyong Kim received his BS degree from Daegu Gyeongbuk Institute of Science and Technology (DGIST), Republic of Korea, in 2018. He is currently working toward his integrated MS/PhD degree under the supervision of Professor Su-Il In at DGIST. His current research interest lies in photo/electrochemical devices and catalyst development for energy and environment applications.

Dowon Bae is a Senior Lecturer at Wolfson School of Mechanical, Electrical, and Manufacturing Engineering, Loughborough University (UK). He received his BSc & MSc (both Summa cum laude) from the Russian State Technological. After industrial R&D activities at LG Innotek, he obtained a PhD in Physics at the Technical University of Denmark in 2015. He also worked at the Delft University of Technology as a Marie-Curie Postdoc Fellow until 2020. Prior to his academic experience at Loughborough University, he was an Assistant Professor at Heriot-Watt University (UK, 2020cm3). His research interests include solar and thermal energy conversion *via* electrocatalytic and electrochemical systems.

Su-Il In is a professor at DGIST, Republic of Korea. He received his Ph.D. in 2008 from the University of Cambridge, UK. He served as a postdoc at the Technical University of Denmark and Penn State University (2008–2012) and later as a visiting scholar at the Department of Environmental Science & Engineering at Caltech, CA, USA (2019–2020). His current research interests are focused on energy and environmental issues, including photo/electrocatalytic CO_2 conversion, betavoltaic cells, nano-bio hybrid technology, and microbial fuel cells.

Table of Contents

Considering the progress of the photoelectrochemical (PEC) conversion of CO_2 into useful chemical products, different materials have been studied in recent years. The elemental doping to electrode materials tunes their photoelectronic properties through the incorporation of impurities, creating defect states that result in band gap tuning, expanded light absorption, enhanced charge separation, and improved CO_2 adsorption capability. In this regard, this review comprehensively summarizes the progress of elemental-doped photoelectrode materials for PEC CO_2 reduction.